Effects of the Purkinje system and cardiac geometry on biventricular pacing: a model study

---

Daniel Alberto Romero García

A document submitted in partial fulfillment for the masters degree in information, communication and audiovisual media technologies (TICMA).

Department of Information and Communication Technologies, Universitat Pompeu Fabra.

Typeset by the author using LaTeX2e.

Effects of the Purkinje system and cardiac geometry on biventricular pacing: a model study

Daniel Alberto Romero García

September 2009

Supervisor: Dr. Alejandro F. Frangi

co-Supervisor: Dr. Rafael Sebastián

Department of Information and Communication Technologies
Universitat Pompeu Fabra

Acknowledgements

I would like to express my appreciation for the guidance and collaboration received from the coauthors of this study. Throughout its progress, the tutoring skills of Dr. Sebastián and Dr. Zimmerman have nurtured the scientific spirit in me. The seniority of Dr. Frangi and Dr. Bijnens were fundamental in directing the goals and addressing methodological aspects of the research. The external collaboration with Dr. Vigmond and Mr. Boyle, PhD student, contributed to the team the expertise in cardiac modeling. The author also acknowledges the contributions from Dr. Plank to the *SPIE'08* proceedings paper. The interaction with all them has been a delightful research and life experience.

Abstract

Heart failure leads to gross cardiac structural changes. While Cardiac Resynchronization Therapy (CRT) is a recognized treatment for restoring synchronous activation, it is not clear how changes in cardiac shape and size affect the electrical pacing therapy. This study used a human heart computer model which incorporated anatomical structures such as myofiber orientation and a Purkinje system (PS) to study how pacing affected failing hearts. The PS was modeled as a tree structure that reproduced its retrograde activation feature. In addition to a normal geometry, two cardiomyopathies were modeled: dilatation and hypertrophy. A biventricular pacing protocol was tested in the context of atrio-ventricular block. The contribution of the PS was examined by removing it, as well as by increasing endocardial conductivity. Results showed that retrograde conduction into the PS was a determining factor for achieving intraventricular synchrony. Omission of the PS led to an overestimate of the degree of electrical dyssynchrony while assessing CRT. The activation patterns for the three geometries showed local changes in the order of activation of the lateral wall in response to the same pacing strategy. These factors should be carefully considered when determining electrode placement and optimizing device parameters in clinical practice.

CONTENTS

I. Introduction

This section includes brief definitions on the basics of cardiac physiology and cell modeling intended for a reader new to the topics. Although description of specific cardiac pathologies modeled in this paper are also presented here, a thorough report of cardiac pathophysiology and cardiac modeling is not within the scope of the present work. The reader with expertise in these fields is suggested to go to Section I-D, which addresses the state of the art and the need for a model study on the role of the Purkinje system and cardiac geometry during pacing. Section I-E gives a methodological overview of the work presented here.

A. Heart anatomy and physiology

Life in the human body is sustained by the synchronous interaction of all organs. In this team work the heart plays an important role. Its function is to pump the blood around the body to deliver nutrients and neurochemical signals to other tissues, and at the same time it collects waste products from them.

At visual inspection, four main structures in the heart are distinguished: two upper chambers called atriums and two lower chambers called ventricles (see Fig. 1). The outside surface of these chambers is called epicardium and the inside surface is called endocardium. The atriums, with a thin layer of muscle, function as recipients for the blood returning to the heart. The ventricles, much thicker than the atriums, are the actual pumps responsible of putting the blood into circulation.

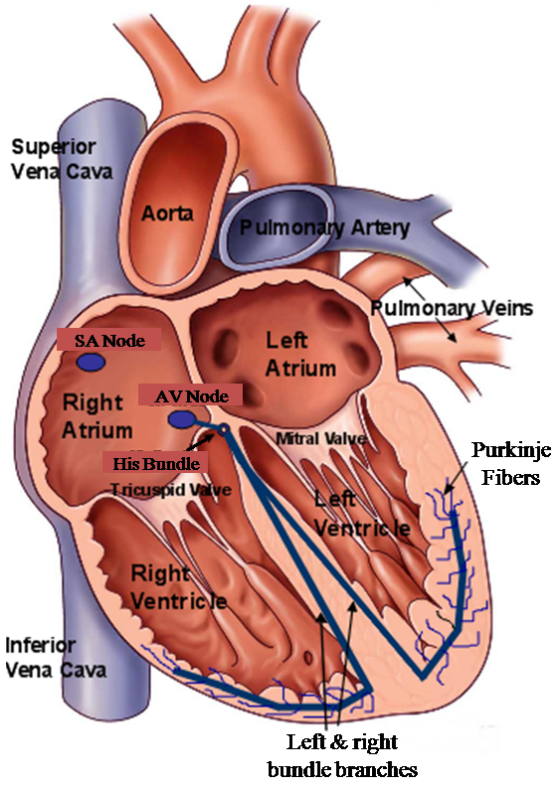

Fig. 1. **Heart anatomy and the conduction system**. Anatomical view of the heart structures and the components of its electrical conduction system (in blue). From www.washingtonhra.com.

The compartments discussed above divide the heart in two: a right heart made by the right atrium (RA) and the right ventricle (RV), and a left heart made by the left atrium (LA) and the left ventricle (LV). Right heart and left heart circulations are kept isolated by the interatrial and interventricular septum. The only connection points among

the four chambers are the mitral valve, regulating the blood flow from LA to LV, and the tricuspid valve regulating flow from RA to RV.

At a histological level, the architecture of the cardiac muscle (myocardium) in the ventricular wall is arranged in fibers and sheets. The fibers run circumferentially inside the wall changing their inclination angle from the inner surface of the ventricle (endocardium) to the outer surface (epicardium) from 50° to -60° respectively [1] (see on Fig. 5 a model representation). The electric impulse, which regulates cardiac contraction by its transmission from cell to cell, is strongly dependent on fiber direction; the conductivity is at its maximum when transmitted longitudinal to the fiber while at its lowest transversally [2].

The cells conforming the heart muscle are called cardiac myocytes. They are specialized contractile and excitable cells, capable of transmitting an electrical impulse to neighboring cells at a velocity of $0.4m/s$. Moreover, the heart has also a specialized fast conducting tissue responsible for the synchronous activation of the myocytes during the cardiac cycle. The cells forming this tissue are called Purkinje fibers and can conduct the electrical impulse at $4m/s$ [2], [3].

The electrical activation triggers the contraction. The natural pacemaker is located in the sinoatrial node in the RA. From there the activation spreads inside the atrium reaching the atrioventricular (AV) node. The AV node, in healthy hearts, is the only electrically conducting point from the atriums to the ventricles. An important function of the AV node is to delay the electrical signal to give time to the atriums to contract and pump blood into the ventricles before these contract. Coming out from the AV node is the bundle of His which branches to form the left and right bundle branches that innervate their corresponding ventricle. Beneath the ventricular endocardium, the bundle branches connect to the Purkinje system (PS), a network of fibers that transfer the electrical impulse to numerous myocytes. It is important to highlight that the conduction system is electrically isolated from the surrounding myocardium. The terminal fibers of the PS are the only electrical contact points between the PS and the myocytes. These terminal fibers are called Purkinje-myocardial junctions (PMJ) [4], [5].

B. Heart failure

Heart failure (HF) is a condition in which the heart is unable to fulfil the blood requirements of the body. The poor cardiac performance limits the physical activity a patient can do without discomfort. More than a disease in itself, the term HF is assigned to the effects of an underlying group of diseases. Depending on the clinical condition of the patient, HF can be a combination of pathologies. Examples are coronary artery disease, left bundle branch block, dilated cardiomyopathy (DCM), and hypertrophic cardiomyopathy (HCM). The last two diseases involve a remodeling process on the ventricular walls. In clinical practice, DCM is diagnosed when the ventricular diameter exceeds 117% of the expected normal, age-adjusted value and HCM is diagnosed when wall thickness exceeds 125% of the expected maximal thickness [4].

1) Cardiac resynchronization therapy: Cardiac resynchronization therapy (CRT), a pacemaker therapy, is used as treatment on end stage HF. Different from other pacing modalities, it uses three pacing electrodes placed in the RA, RV endocardium apex and the LV free wall epicardium (see Fig. 2). The RA electrode can be used only for sensing or pacing depending on the pathologic condition. The concept behind CRT is to restore synchronicity in the contraction pattern of the ventricles by applying electrical charges.

CRT improves systolic (contraction) function in ventricular dyssynchrony [6], leading to amelioration of functional capacity, inverse remodeling, and reduction of morbidity and mortality [6]–[8]. Studies have shown beneficial outcomes in patients with DCM [9] and HCM [10]. Nevertheless, previous population studies on CRT showed that about a third of patients do not respond favorably to the treatment. As possible causes for this it has been pointed out suboptimal device setup and electrode positioning.

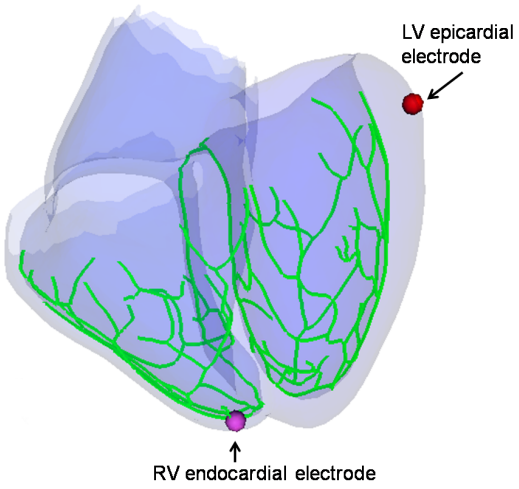

Fig. 2. **Position of CRT electrodes on the ventricles**. The arrows indicate the electrode positions. The LV electrode lies on the epicardium. The RV electrode is on the endocardium at the apex region. From www.washingtonhra.com.

C. Modeling of cardiac electrophysiology

Modeling cardiac electrophysiology involves two main steps, first, calculating the underlying variations in ionic concentrations across the cellular membrane at each node in the domain, and second determining the dynamics of electrical activity at tissue level.

1) Ion dynamics: Cardiac cells (myocytes) are a special type of excitable cells. The ionic concentrations inside and outside the cells are kept unbalanced under resting conditions, generating a transmembrane potential gradient. The pores in cell's membrane are responsible for maintaining the difference by passive and actively transporting molecules across it.

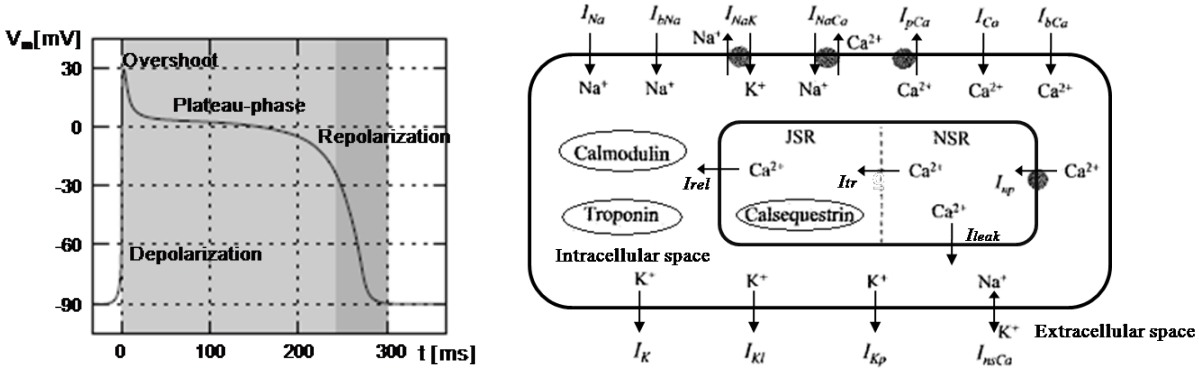

Fig. 3. **Action potential plot and a schematic cell model**. a)The action potential begins from a resting potential of about -90 mv. A very steep slope marks the depolarization phase which rises the potential up to 30 mv. Calcium currents are responsible for the plateau phase, after which repolarization returns the cell to its resting state (from [5]). b) Schematic diagram of the second Luo-Rudy (1994) ionic model (from [2]. Also find there further details). The model describes in detail intracellular calcium dynamics.

A change in the membrane potential, as in the case of an applied electrical stimulus, can cause the depolarization of a cell if the change in potential exceeds a certain threshold. The term depolarization designates a series of processes by which the conductance of the pores on the membrane change to create a rapid flux of positive ions into the cell. The reestablishment of the resting conditions is called repolarization, and is the process in which the cell evacuates ionic excesses. The cycle of depolarization and repolarization of a cell is called action potential (see Fig. 3). The action potential of cardiac cells is different from other excitable cells (i.e. nerve and skeletal cells).

Myocytes stay depolarized for a significant period of time creating what is called a plateau phase in their action potential [3]. Calcium intake is the main ion responsible for the plateau and it is also responsible for achieving the mechanical contraction. Therefore during plateau phase the cell remains contracted.

The reproduction of an action potential is the focus of electrical cell models. Most single cell models are developed to describe the ion dynamics across membrane and regulation inside the cell (see example of the second Luo-Rudy ionic model (1994) in Fig. 3), although some have appealed to simplified polynomial representations [11] omitting the subcellular processes. Complex electrophysiological cell models are based on experimental measurements and have proven to represent with sufficient accuracy the actual behavior of cardiac cells. The majority of these ionic models use as building blocks the formulation proposed by the Hodgkin-Huxley model for the ionic currents. The latter won the Nobel Prize in 1963 for their model describing the action potential of the squid giant axon. Given the importance of this model, its main features will be explained next briefly.

The Hodgkin-Huxley model

Throughout a series of voltage clamp experiments performed on giant nerve axons from a squid Hodgkin and Huxley were able to determine the conductance of the cell membrane to certain ions. They concluded that the conductances are governed by both the transmembrane potential and time. Thus they chose to define the conductances as functions of the maximal conductance and voltage-dependent gating mechanisms, where necessary [2].

The model is composed of three currents: inward sodium current (I_{Na}), outward potassium current (I_{K}), and a leakage current (I_{L}). The motion stated here refers to whether the current is leaving the cells or entering it. The leakage current exits the cells and is an unspecific to an ion specie and also time-independent. The currents are given by:

$$I_{\mathrm{Na}} = \bar{G}_{\mathrm{Na}} m^3 h (V_{\mathrm{m}} - E_{\mathrm{Na}}) \tag{1}$$

$$I_{\mathrm{K}} = \bar{G}_{\mathrm{K}} n^4 (V_{\mathrm{m}} - E_{\mathrm{K}}) \tag{2}$$

$$I_{\mathrm{L}} = G_{\mathrm{L}} (V_{\mathrm{m}} - E_{\mathrm{L}}) \tag{3}$$

where $\bar{G}_{\mathrm{X}}$ is the respective maximum conductances for each current, while the E_{X} is the corresponding Nerst equilibrium potential or also called the reversal potential for the ionic species. The variables m, h and n are responsible for the opening and closing of an ion channel. They are also referred to as gating variables and are time-dependent. In a general form, if y is the gating variable for ion X, its time dependence is determined by:

$$\frac{dy}{dt} = \alpha_{\mathrm{y}}(1 - y) - \beta_{\mathrm{y}} y \tag{4}$$

where α_{y} and β_{y} are rates of opening-closing respectively, and are voltage dependent variables. y accounts for the probability of finding channel X open.

Now, for the sodium current (1), the data was found to fit the best using three activation gates (m) and one inactivation gate (n). The alphas and betas were fitted to the experimental data, resulting in the following equations:

$$\alpha_{\mathrm{m}} = \frac{0.1(V_{\mathrm{m}} + 25)}{exp[0.1(V_{\mathrm{m}} + 25)] - 1} \tag{5}$$

$$\beta_{\mathrm{m}} = 4exp\left[\frac{V_{\mathrm{m}}}{18}\right] \tag{6}$$

$$\alpha_{\mathrm{h}} = 0.07exp\left[\frac{V_{\mathrm{m}}}{20}\right] \tag{7}$$

$$\beta_{\mathrm{h}} = \frac{1}{exp[0.1(V_{\mathrm{m}} + 30)] - 1} \tag{8}$$

The n gating variable is define in a similar way. This is the basic form in which posterior models were postulated. They have gating mechanisms with corresponding rate variables with much more detailed ionic transport across the membrane. For further reading on gating mechanisms and the Hodgkin-Huxley model see [2], [3].

2) Tissue model: One of the most widely known models for electrical propagation in cardiac tissue is the bidomain model [12]. In this model the tissue is divided into two domains: intracellular and extracellular. Both domains are separated by the cell's membrane and each of them have their own potential. Its continuous (volume averaged) approach accounts for intercellular connectivity by gap junctions. These are porous structures that interconnect cells allowing cellular communication and signal transmission [3].

The intracellular and extracellular potential fields are described through linked membrane behavior in the following equations:

$$\nabla \cdot (\bar{\sigma_i} + \bar{\sigma_e})\nabla\phi_e = -\nabla \cdot \bar{\sigma_i}\nabla V_m - I_e \tag{9}$$

$$\nabla \cdot \bar{\sigma_i}\nabla V_m = -\nabla \cdot \bar{\sigma_i}\nabla\phi_e + \beta I_m \tag{10}$$

$$I_m = C_m\frac{\partial V_m}{\partial t} + I_{\text{ion}} - I_{\text{trans}} \tag{11}$$

where $\bar{\sigma_i}$ and $\bar{\sigma_e}$ are respectively the intracellular and extracellular conductivity tensors, defined in the transverse and longitudinal directions, β is the surface-to-volume ratio of the cardiac cells, C_m is the capacitance per unit area, ϕ_i and ϕ_e are respectively the electrical potentials in the intra and extra cellular spaces, V_m is the transmembrane voltage ($\phi_i - \phi_e$), and I_{ion} is the current density flowing across the cellular membrane. I_{trans} is the transmembrane current density stimulus as delivered by the intracellular electrode and I_e is an extracellular current density stimulus. Note that the bidomain equations are a continuum approach that homogenize the media. Eq. 9 is an elliptic equation and Eq. 10 is a parabolic equation. Eq. 11 is a set of ordinary differential equations which can be solved independently for each node in the domain using finite element methods.

In [13] it was shown that there are extremely small differences between the potentials obtained with bidomain and monodomain models, both for depolarization and repolarization. In the monodomain equation only the parabolic part of the bidomain equation (Eq. 10) needs to be solved with a conductivity tensor given by $\sigma = \sigma_i(\sigma_i + \sigma_e)^{-1}\sigma_e$. This is a convenient approach that reduces the amount of computational time needed for each simulation. Even so, solving the monodomain equation in large fine meshes using short time steps is computationally expensive. Increasing the time step or the mesh discretization to speed up the simulations can be problematic when solving the bidomain or monodomain equations since the maximum possible time step length is constrained not only by theoretical accuracy but also by stability considerations [14]. The use of semi-implicit methods allows for an increase in the maximum stable time step, but the dependency on spatial resolution remains a factor.

D. Heart modeling

As the use of whole heart computational models for electrophysiological simulations becomes more feasible [13], [15], they are starting to be considered as a practical way to explore certain phenomena that are difficult to study *in vivo*. Various computational studies have undertaken the task of unveiling pathological substrates and assessing treatment methodologies. Current available cardiac models, ranging from single cell [16]–[18] to tissue level [19], [20] and organ level [21], [22], are sufficiently accurate to model complex processes, including ion kinetics in healthy and pathological conditions. In many cases, cardiac modeling can be used to investigate phenomena such as drug effects on the electromechanical response and arrhythmogenesis [19], [23].

Although cardiac geometry can be extracted from existing image modalities, many other features important to the modeling process (i.e. myofiber orientation, tissue conductivity) cannot be non-invasively obtained; thus, population based data is used instead. Such is the case for the Purkinje fibers, the fast conducting cardiac tissue responsible for synchronous activation of the ventricles during the cardiac cycle. Despite its relevance, its structure and effects are commonly not considered in cardiac simulations [24]. Previous studies have attempted to model the Purkinje system (PS) following anatomical landmarks based on maps of the activation sequence. These maps helped determine roughly the Purkinje myocardial junctions (PMJ) [25]. In some electrical modeling studies researchers have estimated a time delay function for stimulating a number of nodes on the endocardium to reproduce the depolarizing pattern of the PS [22], [26]. Others have used high subendocardial conduction velocities to represent the PS influence [27]. These approaches to incorporating PS functionality through bypassing its specific modeling is problematic because it disables an intrinsic property of the PS: retrograde conduction. Bidirectional electric flow along the PS might not be necessary for normal sinus activation of a healthy heart, but its contribution is important during analysis of CRT, where the electrodes are positioned close to the distal portion of the PS.

Another factor to bear in mind during evaluation of CRT candidates with heart modeling is the geometry of the ventricles. Heart failure patients can suffer from pathological conditions that lead to ventricular remodeling. Such are the cases of dilated cardiomyopathy (DCM) and hypertrophic cardiomyopathy (HCM). Previous model studies on paced hearts include work focused on the electromechanical effects of pacing each ventricle [28], or optimizing CRT pacemaker settings based on electrical information [24], but the retrograde conduction of the PS has not been accounted for.

Understanding the activation sequence for a particular patient, given the geometrical characteristics and knowing the effect of the underlying structures, could facilitate selection of appropriate treatments and tailor the CRT devices to optimize therapeutic outcome on an individual basis.

E. Aim and overview of the study

The study presented in this paper aims to elucidate changes in the activation pattern due to the interaction of CRT pacing and the PS in normal and pathological human hearts by means of a heart model.

A BV mesh from a subject with no underlying cardiac disease was used. This mesh was previously obtained with a statistical model-based approach from a set of multislice computed tomography (MSCT) images [29]. Through mathematical transformations the original mesh has been deformed to emulate a DCM and HCM anatomies. The geometrical models were used to simulate electrical activation under normal sinus rhythm and paced conditions in the context of a third degree atrioventricular (AV) block. Complete blockage of AV conduction leaves the task of ventricular activation to the pacemaker alone. For each element in the volumetric meshes the fiber orientation was computed based on Streeter's description [1].

Electrical propagation in cardiac tissue was modeled using the monodomain formulation, and a 1D cable model for the PS. For BV pacing, the pacemaker electrodes were modeled as current injection points at certain sites of the

geometries. A pacing protocol was defined using different sequential pacing strategies (interventricular delays), to understand how histological structure and geometry affects cardiac activation for different pacemaker configurations. For each geometry, each pacing protocol was performed with and without the PS. Furthermore, models without PS and increased conductivity at the endocardium were used to represent a dense PS.

A preliminary study with no Purkinje system was published in the conference proceedings of SPIE Medical Imaging 2008 (see VI). Part of the work presented here was published in the lecture notes of computer science of the Functional Imaging of the Heart (FIMH) 2009 (see V). The work presented for the master thesis has been submitted to an impact journal in biomedical engineering and has as an extension the electrical pattern analysis of models with increased endocardial conductivity.

II. Materials & Methods

A. Anatomical models

1) Segmentation and generation of the healthy model: A human anatomical model built from an MSCT image stack obtained from a subject with no underlying cardiac diseases was used. The patient-specific geometrical segmentation was generated using a statistical atlas with a point distribution model and an active appearance model. The atlas was built and trained using 100 MSCT scans from healthy subjects and patients with pathological cardiac conditions [29]. Its use replaced manual delineations by a model based method. On top of the shape model, a number of functional substructures and properties were incorporated onto the atlas. These add-ons include the specialized electrical conduction pathways in the ventricles, i.e. the PS, and anatomical labeling. The endocardium and epicardium of the right and left ventricles were automatically segmented and landmarked from the patient scan to obtain a BV surface triangular mesh.

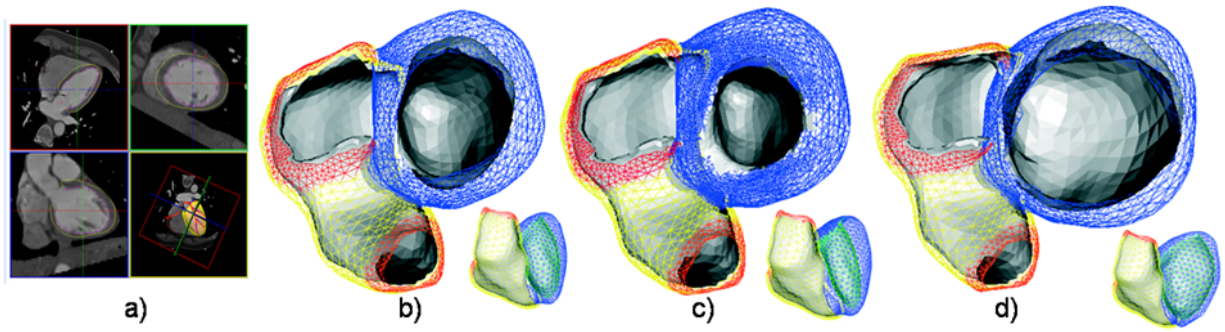

Fig. 4. **Segmentation and ventricular models**.(a)Segmentation process. Basal views of (b) a healthy human ventricle segmented from MSCT. Meshes in (c) HCM and (d) DCM are virtually generated from the original healthy case. All cases include the LV (blue) and RV (yellow), where epicardium is represented as a mesh and endocardium as solid surfaces.

The surface mesh was used afterwards as a boundary to create the fine volumetric tetrahedral mesh needed for the numerical simulation. The use of this type of mesh allowed for the accurate representation of both ventricles and made adaptive mesh refinements possible. Volumetric mesh quality was ensured by controlling both the maximum distance between neighboring nodes and the radius-to-edge ratio to assure regularly-shaped elements. In keeping with recommendations from literature [17], [30], this study used high-resolution meshes with average inter-node distance smaller than $500\ \mu m$ to avoid inaccurate numerical effects such as wavefront warping and other artifacts [31].

The resulting BV, patient-specific mesh had a total of 2.5 million nodes and 15 million tetrahedra, with a mean internodal distance and standard deviation of $496 \pm\ 58\ \mu m$. Fig. 4 (a) shows the anatomical mesh obtained from the segmentation.

2) Generation of pathological anatomies: The original surface mesh obtained from a healthy subject was mathematically transformed into two new meshes, a DCM and a HCM cardiac geometry. The structural disorders were simulated instead of segmented from different patients in order to have a higher control on geometry and to be able to better compare a set of pacing scenarios.

The LV endocardium of the HCM mesh was scaled to achieve a 50% radial increment in wall thickness, reproducing the extent of hypertrophy reported in clinical studies (see Fig. 4 (b)). For the DCM mesh, the right ventricular side of the septum was kept fixed while i) the LV endocardial surface was displaced to obtain a 30% septal thinning; ii) the rest of the endocardial surface was radially dilated to achieve a 50% increment in diameter; iii) the epicardial surface was linearly dilated to maintain a 30% thinning on the average wall thickness with respect to the original value(see Fig. 4 (c)).

Volumetric meshes were generated for all surfaces. The new HCM mesh had 3.5 million nodes and 21 million tetrahedra and the DCM mesh had 3 million nodes and 19 million tetrahedra. The resolution of these meshes were similar to the original, the patient-specific segmented mesh, with average internode distances and standard deviations of 495 ± 51 μm and 450 ± 48 μm for HCM and DCM respectively. The preservation of similar average internode distance avoided undesirable variation in conduction velocities and times between simulations on different meshes.

3) Myocardial fiber orientation: Excitation and recovery sequences are influenced by the direction of myocardial fibers, which determine the longitudinal and transversal orientation of the anisotropic conductivity of intra- and extra-cellular media. Current techniques to obtain the myocardial fiber orientation (such as diffusion tensor magnetic resonance imaging) are unable to non invasively extract myocardial fiber orientation from the beating heart. Therefore, many studies in cardiac modeling use mathematical methods to replicate the rotation of fibers across the ventricular wall [13], [16], [20].

For the present study, the fiber orientation was calculated for every element of the mesh, using a mathematical formulation based on the work of Streeter [1]. In this way, the familiar helical structure of fibers was reproduced, with orientations rotating from 50° at the endocardium to -60° at the epicardium (see Fig. 5).

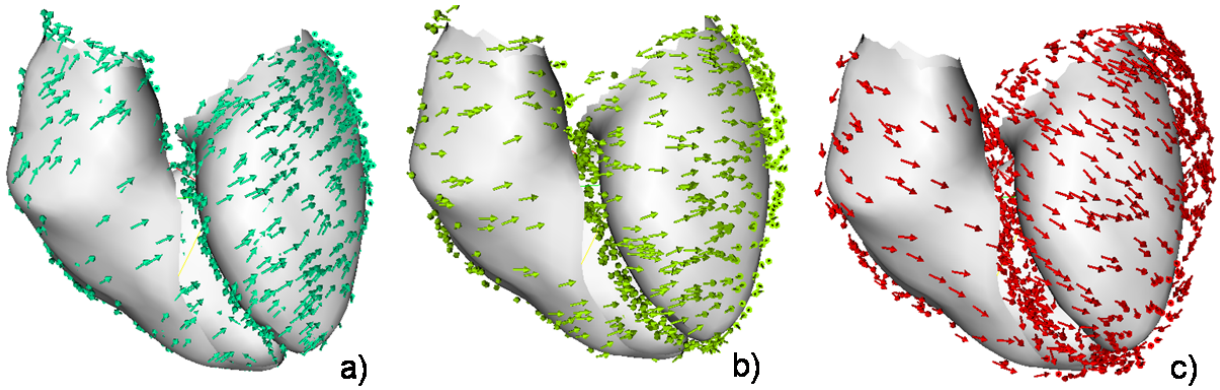

Fig. 5. **Fiber orientation on the myocardial wall**. The fiber orientation is represented by arrows on the model. It is shown at three depths: a) endocardium, b) mid-wall and c) epicardium.

As previously mention, the fiber orientation determines the fast conduction directions, defining an axisymmetric anisotropy. Individual color coded fiber directions can be appreciated at three different depths in the ventricular wall, where the rotation across the ventricular wall is clearly visible.

4) The purkinje system: The PS was manually delineated as an independent structure in the atlas, and fitted to the healthy subject surface mesh during segmentation. Terminals were positioned to reproduce the activation sequence reported experimentally by Durrer [32] and more recently by Ramanathan *et al.* [33]. Paths between terminals were built using splines to form a branching network. The resulting PS model consisted of the bundle branches and 100 segments distributed over the endocardial surface mesh, with no loops in the network. In Fig. 4, the RV (blue) and LV (red) PS are superimposed on the ventricles.

The PS for the pathological meshes was obtained using the previously-described transformation algorithms. It was assumed that in the pathologies modeled, the number of branches in the PS was unaffected and no terminals were generated or destroyed. This is reasonable, considering that in HCM and DCM myocytes and Purkinje cells do not undergo hyperplasia during ventricular remodeling [4].

B. Mathematical modeling

1) Ion dynamics:

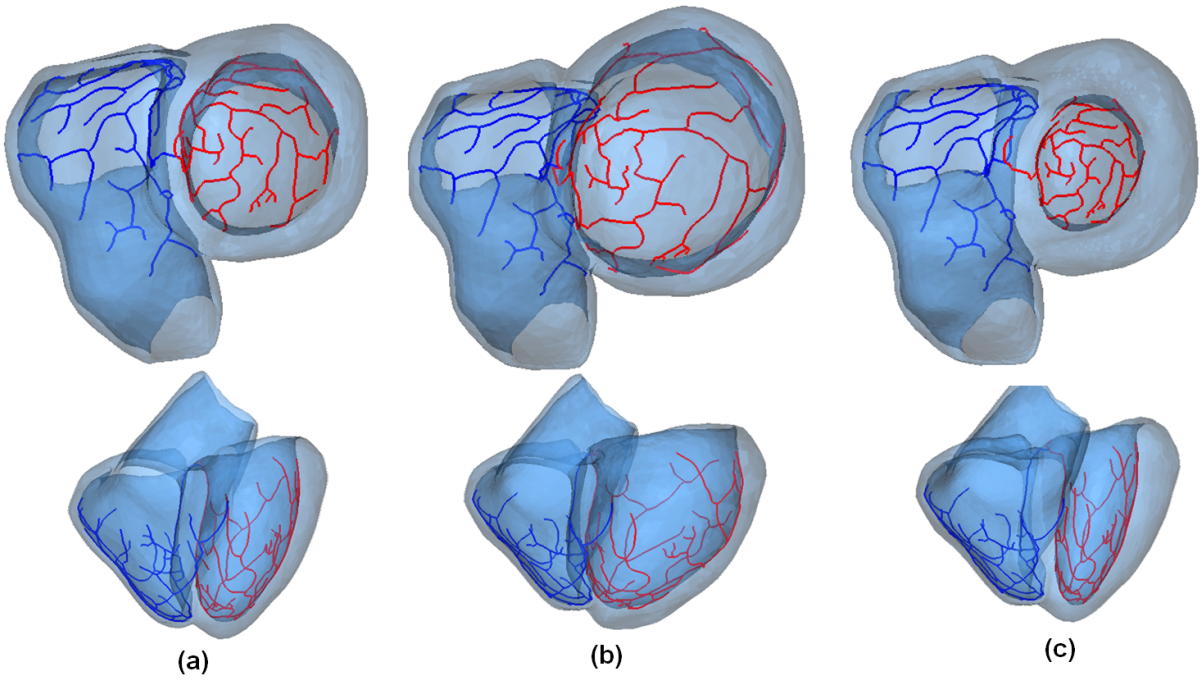

Fig. 6. **Ventricular models**. Basal and anterior views of the biventricular surface models: (a) original healthy subject, (b) dilated (DCM), and (c) hypertrophic (HCM) cardiomyopathies. Solid lines represent the RV (blue) and LV (red) branches of the PS.

- *DiFrancesco-Noble model*: In this study the DiFrancesco-Noble model [34] was used for the PS. Published in 1985, developed on a rabbit heart, was the first model to consider ion pumps and exchangers, concentration changes, and description of calcium transient. The model introduced a formulation for the subcellular process of calcium-induced calcium-release, notion which is still followed in latter models. In the present study it was necessary to augment the conduction velocity to human values by increasing the maximum sodium conductance by a factor of 3.
- *Ten Tusscher and Panfilov reduced model*: In this study the Ten Tusscher et al. model [17] was used to update the transmembrane current of the bulk myocardial cells. The model is the reduce version of their 2004 model [35]. It has nine variables with enough detail to reproduce important arrhythmogenic pathologies. Moreover, the model is four times more efficient that the extended version, important feature in speeding up the computational time.

2) Tissue model: As we are only interested in the activation sequence, we use the monodomain formulation that ignores the extracellular field contribution. The Crank-Nicholson method was used to update transmembrane and extracellular potentials as in [36], since it only requires the solution of a linear system and preserves stability for large time steps. The elements used to represent the bulk myocardium are linear.

3) Cable model for the PS: As in [37], the PS network was constructed from 1D cubic hermite elements to ensure continuity of current at junctions and bifurcations. The fibers were described as 1D cables that branched at certain positions forming a network structure. Purkinje fibers were isolated electrically from the myocardium, and only connected at the terminal points, referred to as Purkinje-myocardial junctions (PMJs). Table I gives the specific parameters used in the cable model, where Ω_{PMJ} is the PMJ resistance and Ω_{PPJ} is the resistance between PS segments, σ is the intracellular conductance, and I_{His} is the current injected into the His bundle to trigger the Purkinje activation.

TABLE I
CONSTANT VALUES USED FOR THE PURKINJE CABLE MODEL

Parameter	Value
Ω_{PMJ}	$27\ M\Omega$
Ω_{PPJ}	$100\ K\Omega$
σ	0.024 S/m
I_{His}	$220\ \mu A/cm^3$

C. Simulation study

The three geometrical models corresponding to healthy, DCM and HCM hearts were used to study the effects of sequential pacing in the activation of the ventricles and its relation to patient-specific geometry and the PS. Sequential pacing is a technique used to determine which is the optimal configuration to activate the RV and LV electrode and obtain the best cardiac output.

The simulation study was designed to assess the impact of the inter-ventricular delay (VVD), between the two pacing electrodes, on the ventricular activation pattern, given a specific position of the BV pacemaker. For every simulation the activation sequence was studied during the first 150 ms after the stimuli. A total of ten scenarios were tested for each geometry, one to reproduce the physiological activation (starting from the AV node), and nine using different pacing strategies that differed in the BV pacemaker VVD. The range of delays used varied from a $30ms$ RV preactivation (VVD -30) to a $50ms$ LV preactivation (VVD 50) with intervals of $10ms$ between pacing strategies. This range of delays encompassed values commonly used in clinical practice. The electrodes of the pacemaker were fixed for all the simulations on the RV apical endocardium and the LV lateral free wall epicardium. The electrodes were modeled as cubes of $1mm^3$ positioned on the bulk myocardium. The electrical stimulus delivered by each electrode was $0.05\mu A/cm^3$ for $1ms$.

In order to further study the contribution of PS to the activation sequence all pacing simulations were repeated in the absence of the PS. Two types of simulations were ran in this context, i) using physiological tissue conductivity values, and ii) using higher conductivities for the bulk myocardial tissue in order to achieve a conduction velocity four times faster. This is a common approximation taken in order to compensate for the lack of PS system.

1) Simulation details: Simulations were performed on an SGI Altix ICE 8200 cluster, with 24 blades inter-connected by an InfiniBand dual-plane fabric. Each blade houses 2 quad-core Intel Xeon 5355 processors at 2.66 GHz. Both electrical properties and ion kinetics were simulated using the Cardiac Arrhythmia Research Package (CARP) [15], [36], [38]. The software allowed for the exploitation of parallel components of the calculation and easily accommodated the establishment of different scenarios. Furthermore, it allowed specifically for modeling of the PS. Each simulation took about 4 hours using blocks of 32 processors.

2) Data analysis: While a cell is not depolarized the membrane potential remains at a resting state. A cell will remain at rest until an external stimulus or an impulse from a surrounding cell induces it to an action potential. The membrane voltage at each node in the volumetric mesh was recorded every $1\ ms$. Using this information, maps of local membrane voltage were build to analyze the activation sequence at selected time frames (see example in Fig. 8). Only the enclosing surface mesh for each geometry was used for visualizing the membrane states given that the intramural activation is not displayed in a 3D projection of the models.

Patterns observed for each pacing scenario and cardiac anatomy were analyzed with cumulative frequency histograms of the amount of activated LV myocardium, similarly as in [40]. Each histogram shows the percentage of LV myocardial tissue activated in time intervals over the depolarization sequence.

In each case, the LV was further analyzed by calculating the mean activation time for each region of the American

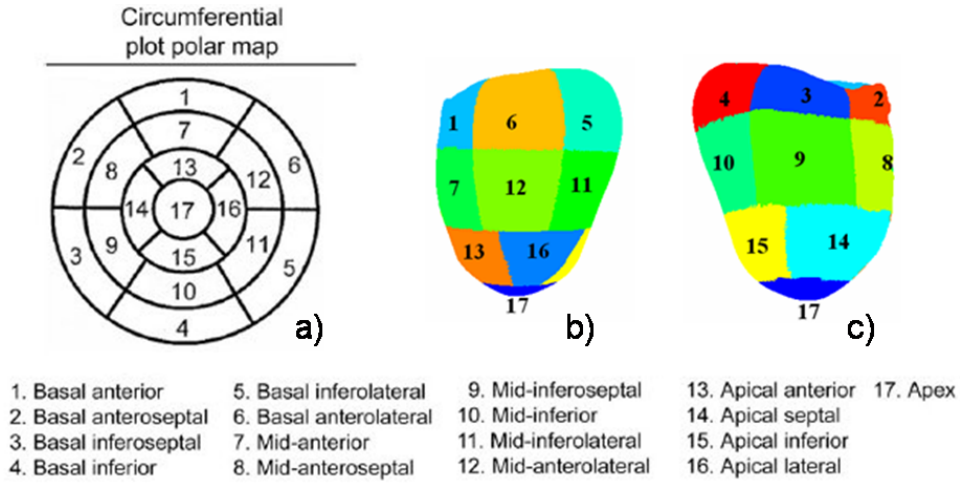

Fig. 7. **The AHA 17 segment model for myocardial segmentation**. a)17 segment hear model, modified from [39]. b) and c) are the antero-lateral and postero-septal views respectively of the 17 segment model in 3D left ventricle.

Heart Association (AHA) standard 17 segment division. Apart from the overall activation pattern that the histograms convey, it is important to consider the spatial order of activation and study whether the LV segments are properly synchronized. These data are important to search for the scenario that shows a better synchrony between the different walls from the point of view of the electrical activation.

III. Results & Discussion

In the physiological simulations, the activation sequence was triggered from the AV node, which activates the bundle of His. The right and left bundle branches propagate the activation to the PS. Since Purkinje fibers are isolated from the myocardium, they only stimulate the tissue through PMJs. The PS initiates as many activation wavefronts on the endocardial surface as there are PMJs on the network, giving rise to a rapid sequence of activation that propagates from apex to base and from endocardium to epicardium, in accordance with previously reported values [32], [41]. The time for all ventricular tissue to depolarize (total activation time; TAT) was computed using the first endocardial breakthrough as a starting point. The values were 90 ms for the healthy heart, 105 ms for HCM, and 119 ms for DCM.

In the case of stimulations triggered by a pacemaker the activation sequence presented significant differences as compared to sinus activations. Snapshots of the evolution of the membrane voltage captured after 10, 60, 100 and 150 ms from the initial stimulus are presented in Figs. 8, 9, and 10. Each figure corresponds to one of the three geometrical models (healthy, HCM and DCM) showing their activation status on the enclosing surface meshes. Therefore, the cuts made on the viewing planes show both the hollow interior and, inside it, the background activations. The biventricular models were paced with simultaneous activation of the pacemaker electrodes. The columns represent models with PS, No PS normal conductivity, and the last one labeled Endo has increased endocardial conductivity replacing the PS. The ventricular walls in the projections are the posterior walls (closer to the backbone) seen from an anterior (chest view) and posterior (back view) position. In the following paragraphs each figure is analyzed separately.

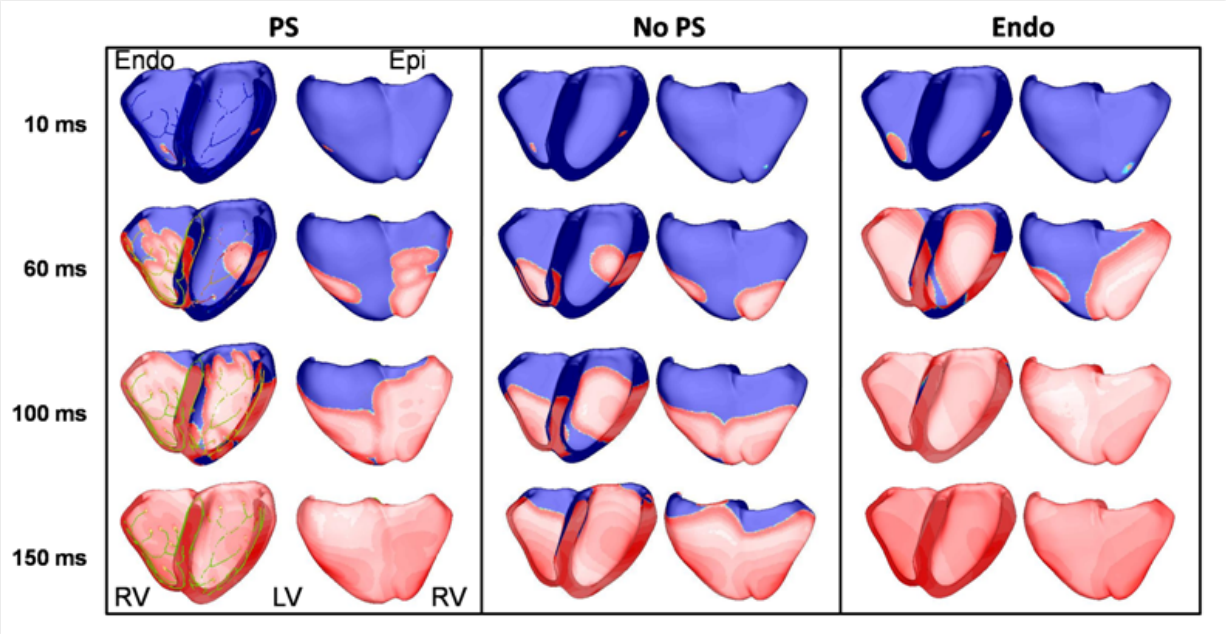

Fig. 8. **Depolarization sequence in the healthy model**. The biventricular models were paced with simultaneous activation of the pacemaker electrodes. The columns represent models with PS, No PS and normal conductivity, and the last one labeled Endo has increased endocardial conductivity. The times displayed are counted after the electrode stimulus. Colors represent the transmembrane potential at each point of the mesh.

Healthy model (see Fig. 8):

- PS: at 10 ms the impulse from the RV electrode found and entered the RV PS. After 60 ms there were widely spread epicardial breakthroughs on the RV, with the RV PS completely activated. The thin myocardial wall of the RV plus the fact that the RV electrode lies on the endocardium (near the PS) were the causes of the RV's

swift activation, as compared to the LV's. The impulse from the LV electrode took longer to find a PS terminal since it had first to travel across the wall (epicardium to endocardium). Thus at 60 ms the electrical impulse was traveling inside the LV PS and the entire structure was not yet depolarized. The action of the LV PS is more clear at 100 ms when the endocardial activation, in contrast to the No PS model, was evenly distributed from apex to base, covering a wider area. This LV endocardial activation had not reached the epicardium yet, whose depolarization so far was attributed to myocardial conduction originated from the epicardial electrode (see Fig. 8, No PS 100 ms). The fast activation of the RV not only contributed to the activation of the septum at all heights but it also participated in the activation of the LV's basal-posterior wall and septal-apical portions.

- No PS: The activation is conducted only through the myocardium following the fiber orientation. This was more evident at 60 ms where the orientation of the activation wavefront at the epicardium had an anterior-basal to posterior-apical direction. In the mean time, at the endocardium the wavefront was oriented antero-apical to postero-basal. Thus isochrones in the epicardium and endocardium formed an *X* shape when overlayed and helped the propagation of the impulse transversally between the layers. Frames 60 and 100 ms show the influence of the RV pacing in the activation of the mid-septum and the LV's septum-apical region. In frames taken at 100 and 150 ms it can be observed that the depolarization of both ventricles occurred in very similar times. Nevertheless, at 150 ms the activation of both ventricles was not finished at basal portions; in the LV those regions were in the lateral wall and the septum.
- Endo: The predominant feature in this activation is the homogeneous and fast diffusion of the two wavefronts from the electrodes. Since the model assumes a highly dense PS distribution at the endocardium the only endocardial breakthroughs are those generated by the pacing electrodes. At 60 ms the activation of the RV was almost finished while a great part of the LV epicardium was not yet depolarized. After 100 ms from the pacing stimulus both ventricles were practically depolarized. In this model it is also important to note that the activation of the septum was greatly attributed to the RV depolarization.

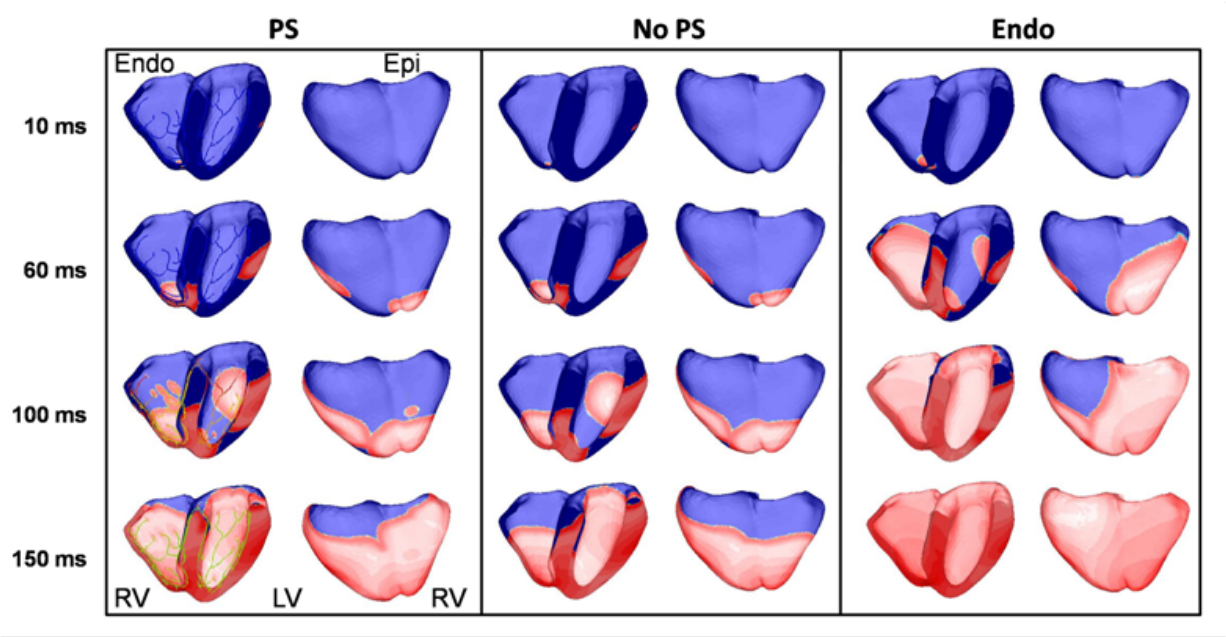

Fig. 9. **Depolarization sequence in the HCM model**. The biventricular models were paced with simultaneous activation of the pacemaker electrodes. The columns represent models with PS, No PS and normal conductivity, and the last one labeled Endo has increased endocardial conductivity. The times displayed are counted after the electrode stimulus. Colors represent the transmembrane potential at each point of the mesh.

Given the detailed description of the healthy model, from here on the explanation of the activation sequences will be focused on the more prominent facts.

HCM model (see Fig. 9):

- PS: At 60 ms the wavefront from the LV electrode had already reached the endocardium and it though still a small wavefront. This remarkable delay is due to thick cavity wall as compared to the healthy model counterpart. At 100 ms the HCM PS was fully depolarized but the wavefronts originated from its terminals were still small. When compared to the healthy PS model activation, the HCM thicker wall imposed a double delay in the activation. The first was the delay in finding a PS terminal after the LV pacing, and the second was the time needed by remote wavefronts to cross from endocardium to epicardium after the PS had spread the electrical activation all over the endocardium.
- No PS: The activation of the epicardium follows the fiber direction but also is influenced in the transverse direction by the transmural activation coming from the endocardium. In the case of the HCM model the transmural contribution to the epicardial activation was less pronounced given the thicker wall. This means that by the time the returning wave from the endocardium was ready to stimulate areas of the epicardium these had already been activated by its original wavefront generated at the pacemaker electrode.
- Endo: At 60 ms the activation of the RV was almost completed. The LV had activated a small portion. At 100 ms there was still a large region of the LV epicardium that had not been depolarized.

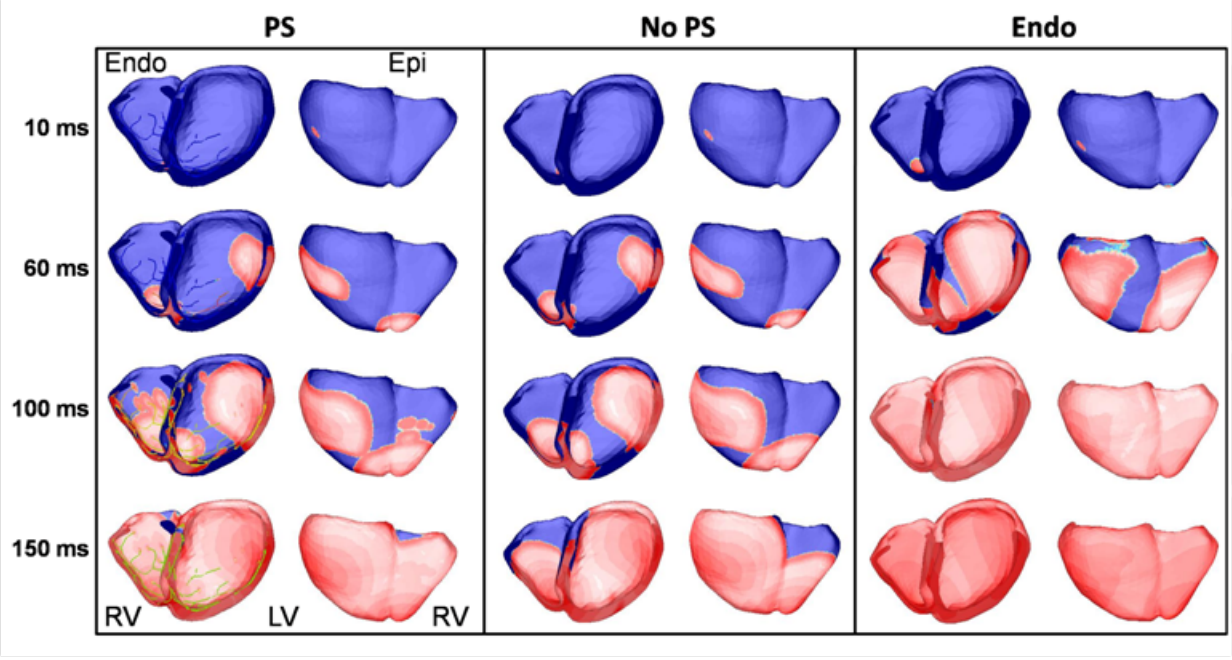

Fig. 10. **Depolarization sequence in the DCM model**. The biventricular models were paced with simultaneous activation of the pacemaker electrodes. The columns represent models with PS, No PS and normal conductivity, and the last one labeled Endo has increased endocardial conductivity. The times displayed are counted after the electrode stimulus. Colors represent the transmembrane potential at each point of the mesh.

DCM model (see Fig. 10):

- PS: The retrograde activation of the LV PS started later than in the healthy model since PS terminals on the endocardium were not nearby the resulting endocardial breakthrough produced by the LV electrode. At 60 ms the PS was still being depolarized, with the majority of its terminal fibers at a resting state. At 100 ms the wavefront on the LV lateral wall had been mainly determined by the myocardial conduction alone. This observation is supported by the fact that on both models of DCM with PS and no PS the activation

wavefront had covered the same volume at this time frame. At 100 ms the LV PS was still activating areas of the endocardium, but by the time its terminal fibers on the lateral wall were activated the wavefront originated from the epicardial electrode had activated the area already. This is due to the thin myocardial wall and the transverse activation contribution from the endocardium in the *X* shaped that contributed to cover this tissue without the help of the PS. Another cause of this was the low density of PMJs, relative to the larger endocardial area of the DCM model. The onset of retrograde activation of the PS was conditioned to the impulse from the LV electrode finding the closest PMJ. Moreover, after entering the closest PMJ, the impulse had longer paths within the PS to travel through before reaching other PS terminals. Thus delaying the activation of remote areas.

- No PS: As explained in the previous paragraph the transverse activation on a thin wall helped the propagation to be fast; faster than in its HCM No PS counterpart. At 150 ms the LV posterior wall was fully activated. Unfortunately the orientation on this figure is not able to display a clearer projection of the LV basal-septal and mid-septal portions which were not depolarize at this time yet.
- Endo: At 60 ms the activation of both ventricles was well advanced. The thin septum allowed the wavefront from the RV electrode to activate the septal-apical region of the LV. This endocardial activation of the LV contributed to diminish its total activation time. On the epicardium of the LV the depolarization was mainly attributed to the transmural activation. The impulse from the LV electrode traveled quickly across the thin wall. The fast depolarization of the endocardium combined with the short time it took to cross the thin ventricular wall are the facts that explain why the return activation from the endocardium overcame the epicardial wavefront.

From the previous analysis it can be drawn that the RV contributes to the septal activation, and it also heavily influences the LV's anterior and posterior wall in all the modeling approaches. Moreover, in models with PS due to the proximity of the RV electrode to the septal wall, the wavefront crosses the septum and contributes to the activation of the LV apex and initiates retrograde activation of the PMJs on the LV endocardium, as seen clinically [42]. RV pacing in models with increased endocardial conductivity also caused retrograde activation of the LV apical endocardium. Consequently, the activation sequence highly depends on the wall thickness and PS distribution on the endocardial surface. Due to our assumption for the PS, for which we fitted a unique structure onto the three geometries, the number of PMJs per endocardial unit area varied between geometries. The HCM, with its smaller endocardial surface, had the highest PMJ density, while the DCM had the lowest. The wavefront on the lateral wall crossing from epicardium to endocardium was faster in the DCM than in the HCM model; however, once on the endocardium, both impulses have to propagate towards a PMJ and, given the density of these, the HCM's wavefront has a higher chance of finding one.

Fig. 11 shows histograms of the percentage of activated LV tissue for three pacing scenarios. Simulations with VVD -30 ms ((a),(d) and (g)) show a period of inactivity on the LV myocardium while the wavefront from the RV electrode reaches the septal wall. On the remaining plots, activation always starts at 0 ms, although this initial excitation is almost imperceptible on the plots because of the very slow rate of initial rise. As activation spreads, the associated curves start to drift apart. For simulations with an underlying PS, Fig. 11 (a)-(c), a high slope represents the contribution of retrograde PS activation. Thus, the wall thickness and the distance to the closest PMJ determine the instant and rate of the major increase in slope on each curve. The LV PS is reached first in the healthy model (solid line), whereas in HCM (dotted) due to the thicker wall and in DCM (dashed line,) due to the lower density of PMJs, there is a higher delay. Simultaneous activation (VVD 0 ms) produced the most uniform results.

Simulations using myocardial models with normal conductivity values but lacking the PS take longer to activate (see Figs. 11 (d)-(f)). The main reason is that the wavefront has to reach remote areas traveling only through bulk myocardium. In Fig. 11(f), the slowest in completing the activation of the LV was the DCM geometry (230 ms)

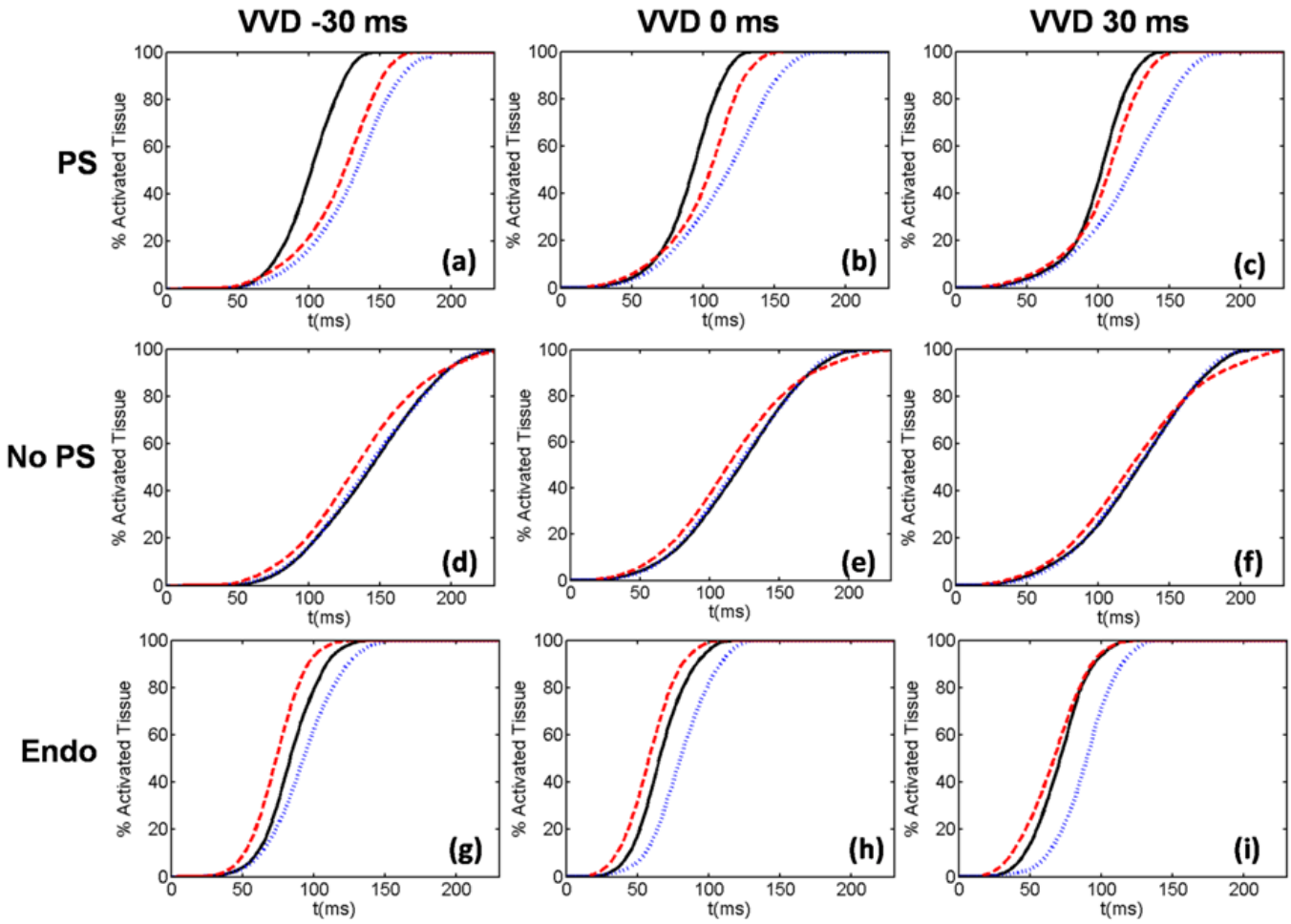

Fig. 11. **Cumulative frequency histograms of the normalized percentage of activated tissue.** The lines correspond to: healthy (solid); DCM (dashed); and HCM (dotted) models. The first row corresponds to simulations with PS while the second and third rows correspond to simulations without the PS and with normal and increased endocardial conductivities, respectively.

the one with the largest circumferential distance to cover, while the Healthy and HCM geometries had finished by about 200 ms. The shapes of the Healthy and HCM curves do not differ significantly.

Another example of the dependence of the activation sequence with the PS distribution is illustrated in Fig. 11(c) (VVD 30 ms). In this figure the curve representing the HCM model (blue; dotted) achieves its maximum slope later than the other geometries. This can be attributed to the fact that retrograde excitation in the HCM occurs later than in the healthy or DCM hearts. While the excitation wavefront is still propagating through the thick ventricular wall in the HCM model, it has already reached a PMJ on the endocardial side in the other two cases. Notably, the trajectory of this curve is nearly indistinguishable from the activation histogram for the HCM heart with no PS (Fig. 11(f)).

In Figs. 11(g)-(i) the curves correspond to models without PS but with increased endocardial conductivity. This implies the assumption that every node on this layer behaves as a PMJ, explaining the very steep slopes of the curves. Moreover, it also implies that the retrograde activation for these models was only dependent on wall thickness. As a consequence, the DCM model, which has the thinnest ventricular wall, was always the fastest to depolarize (shortest TAT), followed by the Healthy and HCM models. Another aspect to note on these simulations is that the depolarization caused by the RV electrode reached the LV apex at the endocardium and initiated rapid activation wavefronts that contributed greatly to LV depolarization. This effect is highlighted in the DCM curves, which

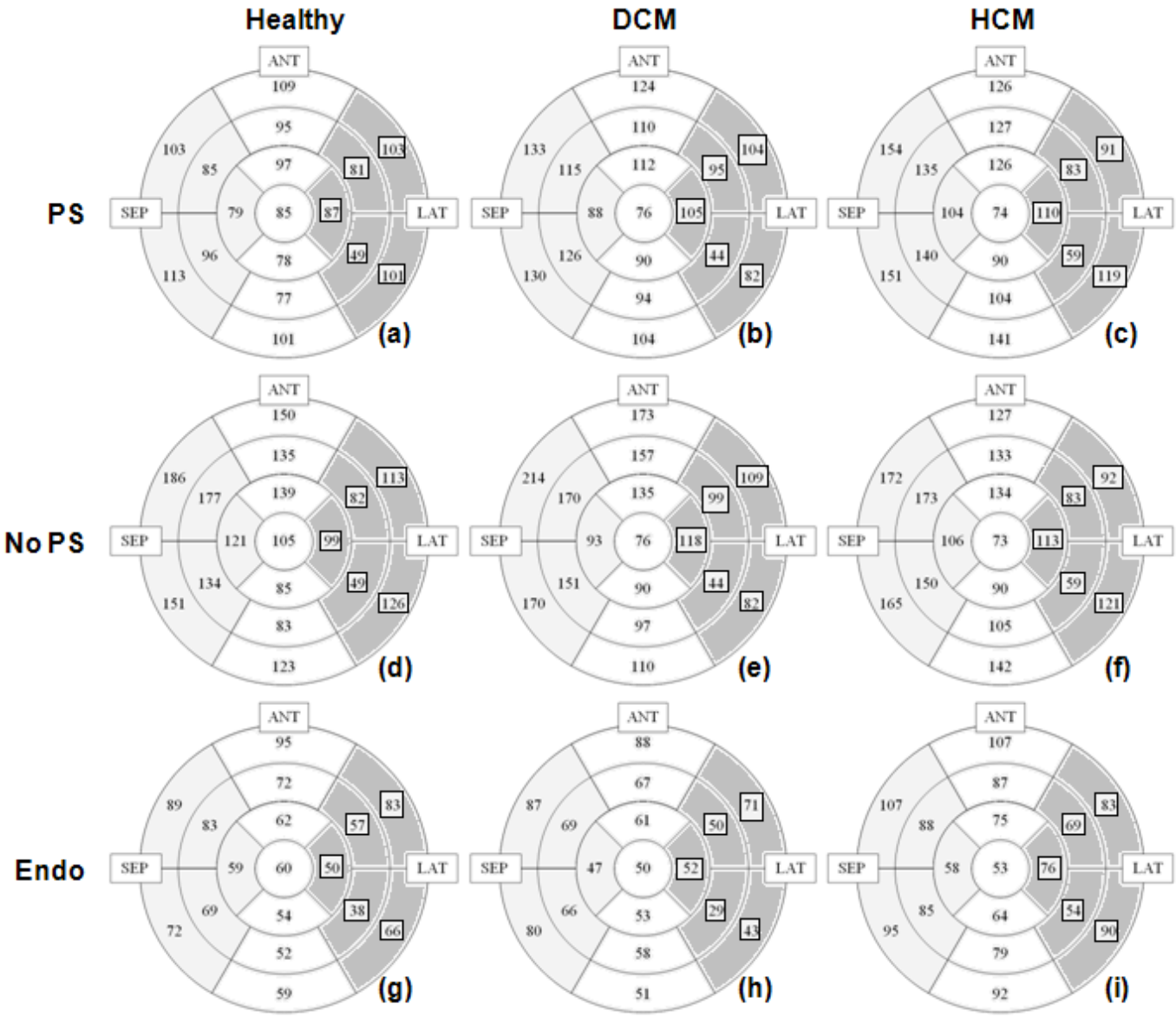

Fig. 12. **Bullseye plots of the AHA 17 segment division, showing LV activation times for simultaneous pacing (VVD 0 ms).** The first row corresponds to simulations with PS while the second and third rows correspond to simulations without the PS and with normal and increased endocardial conductivities, respectively.

tend to move closer to the Healthy curve as the pacing shifts from RV pre-activation to LV pre-activation (see the distance between the dashed and the solid line, which diminishes from Figs. 11 (g) to (i)). Nevertheless, this modeling approach is fundamentally inaccurate, since PMJs are not homogeneously distributed with extremely high density on the endocardium [27], [32]. Therefore the time required to retrogradely activate the PS is neglected.

The bullseye plots (see Fig. 12) correspond to VVD 0 ms with the possible combinations: the three geometries with PS, no PS with normal conductivity values, and no PS with increased endocardial conductivities. Results from models with PS when compared to results from models with an absence of the PS and normal conductivity values indicate that corresponding geometries have very similar mean activation values for the lateral wall (pairs (a)-(d), (b)-(e), (c)-(f)). This highlights the role of the LV electrode alone on this task. In contrast with lateral wall, the septal activation on these plots indicates a significant delay between corresponding models.

Intraventricular dyssynchrony is referred to as a marked delay of the onset of contraction between the septal and

LV lateral wall. One potential treatment is a CRT device with the LV electrode positioned at the site of longest delay. Therefore, the electrical activation as displayed on the bullseye plot conveys information that can be associated to intraventricular dyssynchrony. The analysis of activation sequences across geometries with PS (Figs. 12 (a), (b) and (c)), shows the propagation wavefront on the septal wall always following an apex to base pattern. However, this pattern is lost for the lateral wall activation due to the action of the LV electrode in the mid posteriolateral wall. Moreover, in this region, the order of activation depends on the geometry. Within models lacking the PS but with normal conductivity values (Figs. 12 (d), (e), (f)) the apex to base activation pattern of the septal wall is preserved, although with a significant prolongation in activation compared to with-PS counterparts. This same pattern is observed in models with increased conductivity values (Figs. 12 (g)-(i)) which have the earliest onset and fastest depolarization of the LV's septal and lateral wall.

Our simulations show that the mean activation times of the septum and the lateral wall are more synchronous and physiological in models with PS (see Fig. 12) as compared to models without PS, which highlights the role of the PS in maintaining synchronicity between the walls of the ventricles by minimizing their activation delay. The models with normal conductivity values and no PS showed a prolonged activation on their histograms and an activation widely spread in time when compared to simulations with PS. TAT is associated to the QRS interval, an index that is used to assess the CRT optimization [43]. Thus activated tissue histograms can be interpreted as a global index of intraventricular synchronicity. Simulations with lower intraventricular delays, as displayed on bullseye plots, showed a higher maximum slope and a reduction of TAT.

A. Limitations of this study

The use of computer models to study and predict the response to specific therapies is still in an early stage. The uncertainty of basic physiological constants, coupled with the spatial heterogeneity, is a clear source of concern.

The ionic models used come from two different species. Since only the onset of depolarization was of interest, propagation velocity was of primary importance. To this end, sodium conductance in the PS was adjusted, and junctional parameters were tuned to properly model propagation across the PMJs. Differences in action potential duration between the two ionic models did not affect the results. For future studies involving repolarization, a more realistic human ionic model of Purkinje fibers should be implemented.

Even though we were able to show the importance of the PS in the electrical activation and its effect in CRT, the PS model needs to be improved. The density of terminals in the system is lower than it has been reported in histological studies [44], and therefore delays in the initial activation could be observed. The time to reach the PS from an electrode can be affected by the density of terminals. A specific study to find out a more accurate density and ramification model of the PS remains to be done.

IV. Conclusions

We have presented a cardiac electrical simulation study to assess the importance of anatomical and histological substructures on the paced heart. The computer model includes important substructures, such as the PS and myocardial fiber orientation based on a mathematical formulation. The branching Purkinje structure was approached by manual delineation following anatomical landmarks and its electrical behaviour was modeled as a 1D cable network [37]. The model is able to simulate the electrical activation produced by a BV pacemaker and reproduces the effect of retrograde activation at PMJs.

The results showed that the use of a detailed and sophisticated PS is vital to account in simulations with CRT. Its retrograde conduction property is important to determine the synchronous activation between the LV walls. The usage of models without a PS can over estimate the degree of intraventricular dyssynchrony.

Although while pacing from the epicardium it is not possible to reproduce a physiological pattern, it can however maintain the most electrophysiological resemblance (apex to base) depending on the pathological structure. Applying the same pacing strategy to different models elucidates important local variations, made manifest by differences in activation pattern. Between geometries for a given VVD, the most notable effect on the activation pattern is seen on the lateral wall, where the apical and basal segments changed their order of activation. This should be considered in clinical practice at the moment of the LV lateral wall electrode positioning to improve the outcome of the procedure. Further work on simulations should test different electrode positions to achieve this goal.

REFERENCES

[1] D. Streeter, *Handbook of Physiology: The Cardiovascular System*. Oxford University Press, 1979, vol. 1, ch. Gross morphology and fibrous structure of the heart, pp. 61–112.

[2] A. J. Pullan, M. L. Buist, and L. K. Cheng, *Mathematically modelling the electrical activity of the heart: from cell to body surface and back again*. World Scientific Publishing, 2005.

[3] J. Sundnes, G. T. Lines, X. Cai, B. F. Nielsen, K.-A. Mardal, and A. Tveito, *Computing the electrical activity in the heart*. Springer, 2004.

[4] A. J. Camm, T. F. Lscher, and P. Serruys, Eds., *The ESC Textbook of Cardiovascular Medicine*. Oxford, UK: Wiley-Blackwell Publishing, 2006.

[5] F. Sachse, *Computational Cardiology. Modeling of anatomy, electrophysiology, and mechanics*, ser. Lecture Notes in Computer Science. Berlin, Germany: Springer, 2004, no. 2966.

[6] S. Gassis and A. R. León, "Cardiac resynchronization therapy: strategies for device programming, troubleshooting and follow-up." *J Interv Card Electrophysiol*, vol. 13, no. 3, pp. 209–222, Sep 2005. [Online]. Available: http://dx.doi.org/10.1007/s10840-005-3247-9

[7] W. T. Abraham, "Rationale and design of a randomized clinical trial to assess the safety and efficacy of cardiac resynchronization therapy in patients with advanced heart failure: the multicenter insync randomized clinical evaluation (MIRACLE)." *J Card Fail*, vol. 6, no. 4, pp. 369–380, Dec 2000.

[8] S. Cazeau, C. Alonso, G. Jauvert, A. Lazarus, and P. Ritter, "Cardiac resynchronization therapy." *Europace*, vol. 5 Suppl 1, pp. S42–S48, Sep 2004. [Online]. Available: http://dx.doi.org/10.1016/j.eupc.2004.07.001

[9] P. Castellant, M. Fatemi, E. Orhan, Y. Etienne, and J. J. Blanc, "Patients with non-ischaemic dilated cardiomyopathy and hyper-responders to cardiac resynchronization therapy: characteristics and long-term evolution," *Europace*, vol. 11, pp. 350–355, 2009.

[10] C. A. Rinaldi, C. A. Bucknall, and J. S. Gill, "Beneficial effects of biventricular pacing in a patient with hypertrophic cardiomyopathy and intraventricular conduction delay," *Heart*, vol. 87, no. 6, p. e6, 2002.

[11] P. J. Hunter, M. P. Nash, and D. Noble, "Analytical models of propagation in excitable cells," *Prog Biophys Molec Biol*, vol. 30, pp. 99–144, 1975.

[12] L. Tung, "A bidomain model for describing ischemic myocardial d-c potentitials," *PhD Thesis, M.I.T, Boston, MA*, 1978.

[13] M. Potse, B. Dub, J. Richer, A. Vinet, and R. M. Gulrajani, "A comparison of monodomain and bidomain reaction-diffusion models for action potential propagation in the human heart." *IEEE Trans Biomed Eng*, vol. 53, no. 12 Pt 1, pp. 2425–2435, Dec 2006. [Online]. Available: http://dx.doi.org/10.1109/TBME.2006.880875

[14] E. J. Vigmond, F. Aguel, and N. A. Trayanova, "Computational techniques for solving the bidomain equations in three dimensions." *IEEE Trans Biomed Eng*, vol. 49, no. 11, pp. 1260–1269, Nov 2002. [Online]. Available: http://dx.doi.org/10.1109/TBME.2002.804597

[15] E. J. Vigmond, R. W. dos Santos, A. J. Prassl, M. Deo, and G. Plank, "Solvers for the cardiac bidomain equations." *Prog Biophys Mol Biol*, vol. 96, no. 1-3, pp. 3–18, 2008. [Online]. Available: http://dx.doi.org/10.1016/j.pbiomolbio.2007.07.012

[16] F. H. Fenton, E. M. Cherry, A. Karma, and W.-J. Rappel, "Modeling wave propagation in realistic heart geometries using the phase-field method." *Chaos*, vol. 15, no. 1, p. 13502, Mar 2005. [Online]. Available: http://dx.doi.org/10.1063/1.1840311

[17] K. H. W. J. ten Tusscher and A. V. Panfilov, "Cell model for efficient simulation of wave propagation in human ventricular tissue under normal and pathological conditions." *Phys Med Biol*, vol. 51, no. 23, pp. 6141–6156, Dec 2006. [Online]. Available: http://dx.doi.org/10.1088/0031-9155/51/23/014

[18] D. Noble and Y. Rudy, "Models of cardiac ventricular action potentials: Iterative interaction between experiment and simulation," *Philosophical Transactions: Mathematical, Physical and Engineering Sciences*, vol. 359, no. 1783, pp. 1127–1142, 2001.

[19] C. Henriquez and A. Papazoglou, "Using computer models to understand the roles of tissue structure and membrane dynamics in arrhythmogenesis," vol. 84, no. 3, pp. 334–354, 1996.

[20] A. E. Pollard, M. J. Burgess, and K. W. Spitzer, "Computer simulations of three-dimensional propagation in ventricular myocardium. effects of intramural fiber rotation and inhomogeneous conductivity on epicardial activation." *Circ Res*, vol. 72, no. 4, pp. 744–756, Apr 1993.

[21] D. Noble, "From the hodgkin-huxley axon to the virtual heart." *J Physiol*, vol. 580, no. Pt 1, pp. 15–22, Apr 2007.

[22] E. J. Vigmond, C. Clements, D. M. McQueen, and C. S. Peskin, "Effect of bundle branch block on cardiac output: A whole heart simulation study." *Prog Biophys Mol Biol*, vol. 97, no. 2-3, pp. 520–542, 2008.

[23] B. Rodríguez, L. Li, J. C. Eason, I. R. Efimov, and N. A. Trayanova, "Differences between left and right ventricular chamber geometry affect cardiac vulnerability to electric shocks." *Circ Res*, vol. 97, no. 2, pp. 168–175, Jul 2005. [Online]. Available: http://dx.doi.org/10.1161/01.RES.0000174429.00987.17

[24] M. Reumann, D. Farina, R. Miri, S. Lurz, B. Osswald, and O. Dössel, "Computer model for the optimization of av and vv delay in cardiac resynchronization therapy." *Med Biol Eng Comput*, vol. 45, no. 9, pp. 845–854, Sep 2007. [Online]. Available: http://dx.doi.org/10.1007/s11517-007-0230-x

[25] K. H. W. J. ten Tusscher and A. V. Panfilov, "Modelling of the ventricular conduction system." *Prog Biophys Mol Biol*, vol. 96, p. 152 170, 2008.

[26] P. Colli-Franzone, L. Guerri, M. Pennachio, and B. Taccardi, "Spread of excitation in 3-d models of the anisotropic cardiac tissue. ii. effects of fiber architecture and ventricular geometry." *Math Biosci*, vol. 147, pp. 131–171, 1998.

[27] R. C. P. Kerckhoffs, O. P. Faris, P. H. M. Bovendeerd, F. W. Prinzen, K. Smits, E. R. McVeigh, and T. Arts, "Timing of depolarization and contraction in the paced canine left ventricle: Model and experiment," *(J Cardiovasc Electrophysiol*, vol. 14, pp. S188–S195, October 2003.

[28] R. C. P. Kerckhoffs, P. H. M. Bovendeerd, F. W. Prinzen, K. Smits, and T. Arts, "Intra- and interventricular asynchrony of electromechanics in the ventricularly paced heart," *(J Eng Math*, vol. 47, pp. 201–216, 2003.

[29] S. Ordas, E. Oubel, R. Sebastian, and A. Frangi, "Computational atlas of the heart," in *15th International Symposium on Image and Signal Processing and Analysis*. IEEE Computer Society, 2007.

[30] K. H. W. J. ten Tusscher, O. Bernus, R. Hren, and A. V. Panfilov, "Comparison of electrophysiological models for human ventricular cells and tissues." *Prog Biophys Mol Biol*, vol. 90, no. 1-3, pp. 326–345, 2006. [Online]. Available: http://dx.doi.org/10.1016/j.pbiomolbio.2005.05.015

[31] O. Blanc, N. Virag, J.-M. Vesin, and L. Kappenberger, "A computer model of human atria with reasonable computation load and realistic anatomical properties," vol. 48, no. 11, pp. 1229–1237, 2001.

[32] D. Durrer, R. T. van Dam, G. E. Freud, M. J. Janse, F. L. Meijler, and R. C. Arzbaecher, "Total excitation of the isolated human heart." *Circulation*, vol. 41, no. 6, pp. 899–912, Jun 1970.

[33] C. Ramanathan, P. Jia, R. Ghanem, K. Ryu, and Y. Rudy, "Activation and repolarization of the normal human heart under complete physiological conditions." *Proc Natl Acad Sci U S A*, vol. 103, no. 16, pp. 6309–6314, Apr 2006.

[34] D. DiFrancesco and D. Noble, "A model of cardiac electrical activity incorporating ionic pumps and concentration changes." *Philos Trans R Soc Lond B Biol Sci*, vol. 307, no. 1133, pp. 353–398, Jan 1985.

[35] K. H. W. J. ten Tusscher, D. Noble, P. J. Noble, and A. V. Panfilov, "A model for human ventricular tissue." *Am J Physiol Heart Circ Physiol*, vol. 286, no. 4, pp. H1573–H1589, Apr 2004. [Online]. Available: http://dx.doi.org/10.1152/ajpheart.00794.2003

[36] E. J. Vigmond, M. Hughes, G. Plank, and L. J. Leon, "Computational tools for modeling electrical activity in cardiac tissue." *J Electrocardiol*, vol. 36 Suppl, pp. 69–74, 2003.

[37] E. J. Vigmond and C. Clements, "Construction of a computer model to investigate sawtooth effects in the purkinje system," vol. 54, no. 3, pp. 389–399, 2007.

[38] G. Plank, M. Liebmann, R. W. dos Santos, E. J. Vigmond, and G. Haase, "Algebraic multigrid preconditioner for the cardiac bidomain model." *IEEE Trans Biomed Eng*, vol. 54, no. 4, pp. 585–596, Apr 2007. [Online]. Available: http://dx.doi.org/10.1109/TBME.2006.889181

[39] American Heart Association, American College of Cardiology, and Society of Nuclear Medicine, "Imaging guidelines for nuclear cardiology procedures, part 2." *J Nucl Cardiol*, vol. 6, pp. G47–G84, 1999.

[40] J. Shannon, C. O. Navarro, T. McEntee, G. Riddell, J. A. Adgey, and E. W. Lau, "An early phase of slow myocardial activation may be necessary in order to benefit from cardiac resynchronization therapy," *J Electrocardiol*, vol. 41, pp. 531–535, 2008.

[41] R. J. Myerburg, H. Gelband, K. Nilsson, A. Castellanos, A. R. Morales, and A. L. Bassett, "The role of canine superficial ventricular muscle fibers in endocardial impulse distribution," *Circ Res*, vol. 42, no. 1, pp. 27–35, 1978.

[42] M. W. Kimmel, N. D. Skadsberg, C. L. Byrd, D. J. Wright, T. G. Laske, and P. A. Iaizzo, "Single-site ventricular and biventricular pacing: investigation of latest depolarization strategy." *Europace*, vol. 9, p. 1163 1170, 2007.

[43] S. Kamireddy, S. K. Agarwal, E. Adelstein, S. Jain, and S. Saba, "Correlation of electrical and mechanical reverse remodeling after cardiac resynchronization therapy," *Ann Noninvasive Electrocardiol*, vol. 14, no. 2, pp. 153–157, 2009.

[44] G. K. Massing and T. N. James, "Anatomical configuration of the his bundle and bundle branches in the human heart." *Circulation*, vol. 53, no. 4, pp. 609–621, Apr 1976.

V. APPENDIX I

The Purkinje System and Cardiac Geometry: Assessing Their Influence on the Paced Heart.
Daniel Romero, Rafael Sebastian, Bart H. Bijnens, Viviana Zimmerman, Patrick M. Boyle, Edward J. Vigmond, and Alejandro F. Frangi.
in Proceedings of Functional Imaging and Modeling of the Heart (FIMH'09). 2009, Lecture Notes in Computer Science (LNCS) 5528, pp. 68 77, Springer.

The Purkinje System and Cardiac Geometry: Assessing Their Influence on the Paced Heart

Daniel Romero[1,⋆], Rafael Sebastian[1], Bart H. Bijnens[1,2], Viviana Zimmerman[1], Patrick M. Boyle[3], Edward J. Vigmond[3], and Alejandro F. Frangi[1,2]

[1] Computational Imaging & Simulation Technologies in Biomedicine (CISTIB), Universitat Pompeu Fabra (UPF) and Networking Biomedical Research Center on Bioengineering, Biomaterials and Nanomedicine (CIBER-BBN), Barcelona Spain
daniel.romero@upf.edu
[2] Institució Catalana de Recerca i Estudis Avançats (ICREA), Barcelona, Spain
[3] Department of Electrical & Computer Engineering, University of Calgary, Calgary, AB, Canada

Abstract. Whole heart computer models are being widely used to assess treatment planning like Cardiac Resynchronization Therapy (CRT), a recognized treatment for heart failure. Certain aspects like cardiac geometry and the Purkinje system (PS) are still sometimes neglected on the studies. The present study includes a model of the human ventricles with incorporated anatomical structures such as myofibers orientation and Purkinje system. Two meshes representative of hypertrophic and dilated cardiomyopathies were generated from an original healthy subject mesh. In the context of (III) atrio-ventricular (AV) block, a sequential pacing protocol was tested for different device configurations. The pacing protocols were performed in models including the PS and in models lacking the PS. The results show that the Purkinje System leads to the synchronization of the septum and the left ventricle (LV) lateral wall, thus minimizing the interventricular delay. Also the modifications in the geometry resulted in changes in the activation patterns of the LV lateral wall, differing notably from physiological scenario.

Keywords: Patient-specific geometry, cardiac electrophysiology, Purkinje system, Cardiac Resynchronization Therapy, ventricular pacing.

1 Introduction

Heart modelling is starting to be frequently used to study physiological phenomena as well as to assess therapeutic treatment planning to various cardiac diseases. Furthermore, the integration of patient-specific details may help customize the design of treatments and increase their effectiveness [1,2].

However, a number of anatomical structures and properties (i.e. conductivity of the tissue), needed in the process of modelling, can not be non-invasively

⋆ Corresponding author.

N. Ayache, H. Delingette, and M. Sermesant (Eds.): FIMH 2009, LNCS 5528, pp. 68–77, 2009.

extracted from existing image modalities, and population based data is used instead. This is the case of structures as myocardial fiber orientation and the Purkinje system (PS), key features in the electrical propagation and contraction of the heart. Purkinje fibers form the terminal component of the cardiac conduction system, which is a type of fast conducting cardiac tissue, responsible for synchronous activation cardiomyocytes during the cardiac cycle [3]. Nonetheless, in several electrical and mechanical simulation, and clinical oriented studies, the PS has been neglected [4,5,6,7] thus excluding from their observations and results intrinsic phenomena such as the PS retrograde activation observed in paced hearts.

Cardiac resynchronization therapy (CRT) is a pacemaker therapy used to treat heart failure patients (New York Heart Association class III and IV). It proved to improve systolic function in ventricular dyssynchrony [8], leading to improvement of functional capacity, inverse remodeling, and reduction of morbidity and mortality [9]. Aside from all the benefits, several clinical trials have demonstrated that one third of patients do not respond favourably to CRT using standard clinical selection criteria [9,10]. The use of personalized computational models for electrophysiological simulations of the heart may improve the understanding and application of CRT.

Certainly, comprehending the variations on the activation sequence related to changes in geometry and underlying structures, could help strengthening the selection criteria for CRT and also optimising the pacing protocol for the individual. Thus, the goal of this paper is to study the combined roles of anatomy and PS in the electrical activation sequence on the paced heart through computational simulations.

2 Construction of Anatomical Models

The anatomical models were built using a surface mesh previously obtained from the segmentation of a cardiac multislice computed tomography (MSCT) scan of a healthy subject [11]. For the segmentation, a heart statistical atlas trained and built with 100 MSCT patient scans, and based on point distribution and active appearance models had been used. The models used for the simulations were all biventricular (BV) since general CRT procedures require to implant a pacemaker lead in each ventricle.

The original surface mesh (see Fig. 1(a)) was mathematically transformed into two new meshes to represent dilated (DCM) and hypertrophic (HCM) cardiomyopathies. In clinical practice, dilatation is diagnosed when the ventricular diameter exceeds 117% of the expected normal, age-related, value while hypertrophy is diagnosed when wall thickness exceeds 125% of the expected maximal thickness [12]. Based on these criteria and comparing to typical patients, as seen in the Cardiology clinic, the HCM mesh was constructed by scaling the LV endocardium to achieve a 50% radial increment in wall thickness (see Fig. 1(c)). For the DCM mesh, the LV endocardial surface was radially displaced to obtain a 50% increment in diameter and the epicardial surfaces was consequently dilated

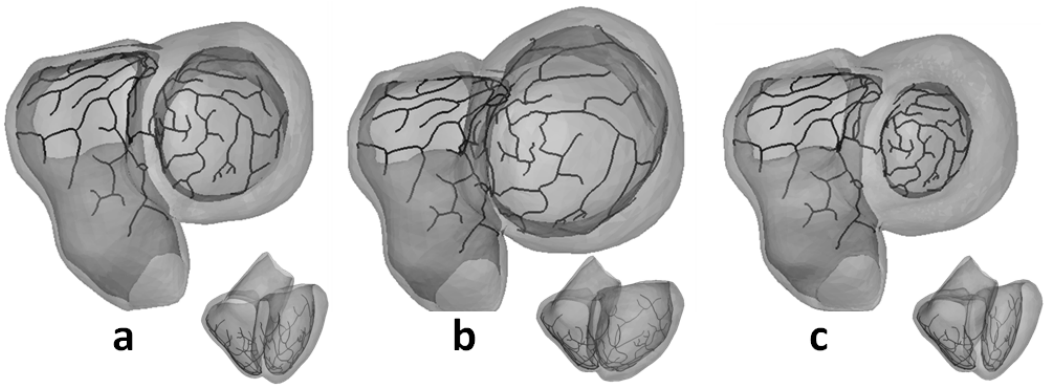

Fig. 1. Basal views of the ventricular surface models: (a) original healthy subject, (b) dilated (DCM), and (c) hypertrophic (HCM) cardiomyopathies. The lines represent the RV and LV PS branches.

to additionally achieve a 30% thinning of the average wall thickness to compensate for the lack of increase in myocardial mass in the dilating (non volume overloaded) hearts (see Fig. 1(b)).

The three surface meshes were then used to create high-resolution volumetric tetrahedral meshes needed for the numerical simulations. Volumetric mesh quality was ensured by controlling both the maximum distance between neighbouring nodes and the radius-to-edge ratio to assure regularly-shaped elements. The average inter-node distance was smaller than 500 μm, and the number of nodes and tetrahedral elements between 2.5 – 3.5 million, and 15 – 21 million, respectively. Mesh resolution was chosen based on a previous study were the influence of the mesh resolution on the electrical propagation [13] was evaluated. Following this study, tissue conductivities values recommended by Roberts [14] with mesh resolutions of the order of 500μm lead to realistic propagation velocities.

For the present study, myocardial fiber orientation was calculated for every element of the mesh, using a mathematical formulation based on the work of Streeter [15].

2.1 The Purkinje System

The Purkinje network was manually defined as an independent structure in the healthy subject surface mesh. The position of the terminals was determined following the experimental activation sequences described by Durrer [3]. The path between terminals were built using splines to form a tree structure. The structure thus obtained consists of the bundle branches and 100 branches distributed over the endocardial surface mesh. In Fig. 1 the RV and LV PS are clearly shown.

The PS in the pathological meshes were obtained using the same transformation algorithms previously described to obtain these deformed meshes. It was hypothesized that in a heart with an abnormal geometry, the number of branches in the Purkinje network is not affected, thereby no new terminals were generated.

3 Mathematical Modelling of Electrophysiology

The electrical propagation in the cardiac tissue was determined using the monodomain formulation [16], with a semi-implicit method (Crank-Nicholson) to iteratively solve the equations [17]. The Ten Tusscher et al. model [18] was chosen to simulate ionic kinetics for bulk myocardial cells, and the DiFrancesco-Noble model [19] for the PS. Both ionic models are based on experimental measurements and have proven to represent realistically the behaviour of cardiac cells.

The PS was modelled as in [20], with 1D cubic Hermite elements to ensure continuity of current at junctions and bifurcations. Purkinje fibers were isolated electrically from the myocardium, and only connected to it at the terminal points by Purkinje to myocardial junctions, which are modelled as fixed resistances. Each Purkinje cell is coupled to the n myocardial elements that lie within a specified radius. For further information see [21]. The pacemaker lead stimulus was modelled as a cube of 1 mm^3 that injects a transmembrane current of 0.05 $\mu A/cm^3$ for 1 ms.

All the numerical calculations were performed using the Cardiac Arrhythmia Research Package (CARP) [22,23].

3.1 Application to Study Electrical Activation in CRT

To assess the influence of cardiac geometry and the PS, a set of sequential pacing protocols were tested on the three cardiac models. Seven pacing scenarios determined by different time delays between the RV and LV pacing leads (interventricular delay, or VVD) were tested. The time delays ranged from 30 ms RV lead preactivation (VVD -30) to 30 ms LV lead preactivation (VVD 30) with intervals of 10 ms between pacing strategies. A (III) AV block was assumed for all these pacing scenarios. Leads were positioned on the apical endocardium (RV lead) and the lateral free wall epicardium (LV lead). As control cases a physiological activation (starting from the AV node) was also performed in the three models.

In order to further study the contribution of PS to the activation sequence all pacing simulations were repeated in the absence of the PS using physiological tissue conductivity values for the bulk myocardial tissue.

4 Results

In the physiological simulations performed for this study, the activation sequences were triggered from the AV node, starting the activation of the bundles of His at time $t = 0$. The activation on the myocardium spreads from the PS terminals to the endocardial surface, and propagates following an apex to base, and endocardium to epicardium pattern.

Figure 2 shows the 3D isochronal maps of the local activation times (LATs) obtained from the simulations, with time intervals of 10 ms. Local activation time is defined as the time, with respect to a reference (i.e. initial lead stimulus), at

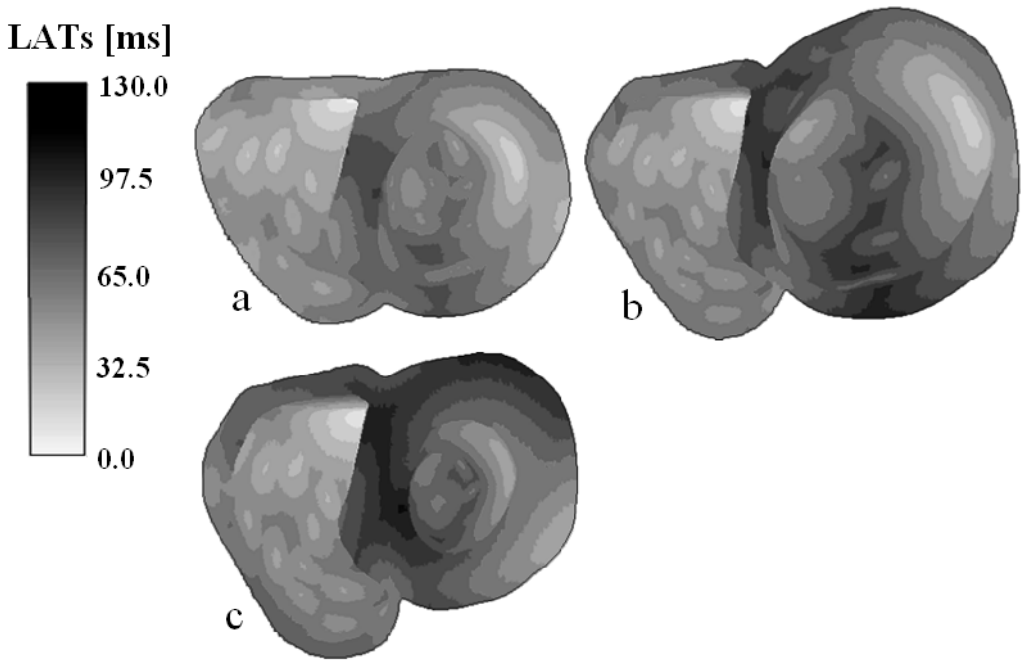

Fig. 2. Basal views showing the 3D isochronal maps of the local activation times for simultaneous pacing (VVD 0). (a) healthy subject mesh; (b) DCM mesh; (c) HCM mesh.

which a cell depolarizes. Figures correspond to activation using simultaneous pacing (VVD 0).

On the pacing scenarios there are two characteristics determining the activation sequences: wall thickness and PS density. The wall thickness, different in the three models, delayed the PS retrograde activation caused by the LV lead stimulus. The wavefront originated from this lead crossed the LV lateral wall and activated the closest Purkinje terminal fiber. Since the area of the endocardial surface varies along the models, being the HCM the smallest, followed by the healthy and the DCM, the density of Purkinje terminals per unit surface depends on the model. This density variation clearly affected the time for LV lead wavefront to find and enter the PS (see differences in late activated regions between Figures 2(a), 2(b), and 2(c)). However, once the PS was retrogradely activated, the depolarization spreaded rapidly, re-entering the bulk myocardium at the remaining terminals of the network allowing the fast activation of remote areas. Although in the models considered the LV lateral wall was mainly activated by the LV stimulus, the activation times of the septal wall were highly sensitive to the use of a PS. The stimulus given by the RV lead entered very quickly the RV PS since the lead rests on the endocardial apical region. Therefore, the activation of the RV PS was completed a few milliseconds after the initial stimulus. This effect can be observed (see Figure 2) as a large number of early activated small regions over the RV endocardium. Moreover, due to the proximity of the RV lead to the septal wall, the wavefront crossed the septum and contributed to the activation of the PS on the LV apex.

In order to further compare the activation patterns obtained for each pacing scenario and cardiac anatomy, cumulative frequency histograms were used. The histograms show the normalized percentage of LV myocardial tissue activated in time intervals, over the whole depolarization sequence.

A common initial activation rate can be observed in the histograms since the activation of the LV spread out initially only through the myocardium (see slope of the curves in Figs. 3 (a)-(c)). In the three models, increments in the activation rate are determined by the amount of myocardium activated from the PS re-entrants, which in turn are dependent on their geometry-density relation, and wavefronts generated by the leads. The LV PS is reached first in the healthy model, whereas in the HCM (solid line) due to the thicker wall, and in the DCM (dashed line) due to the lower density of PS terminals, there is a higher delay. In the case of the DCM, due to the low PS density, the wavefronts travel furthest through the myocardium before finding a PS terminal (lower slope).

Simulations with the models lacking PS show higher values of the ventricle's total activation time (TAT) (see Figs. 3 (d)-(f)). These increased values might

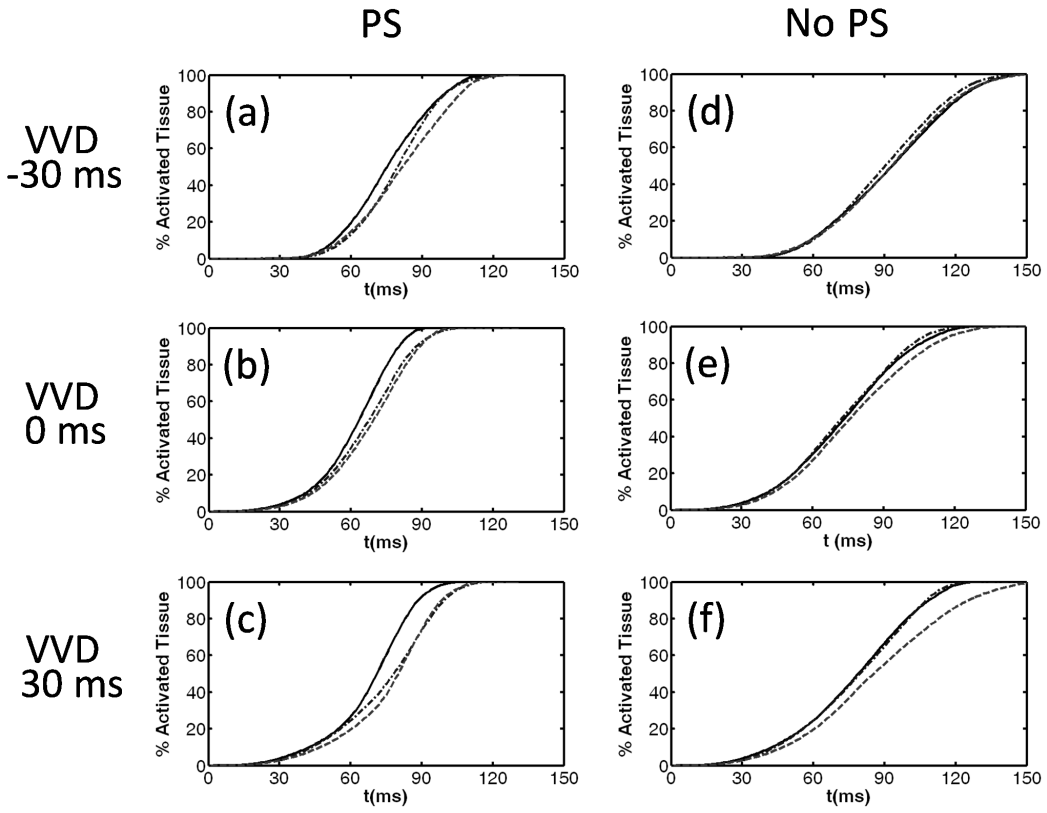

Fig. 3. Cumulative frequency histograms of the normalized percentage of activated tissue. The lines correspond to: (solid) healthy; (dashed) DCM; and (dash-dotted) HCM models. The first column correspond to the simulations with PS, and the second without PS. Rows correspond to RV lead preactivation (VVD -30 ms); simultaneous leads activation (VVD 0); and LV lead preactivation (VVD 30 ms).

lead to intraventricular dyssynchrony on the mechanical response, since different regions are depolarizing with marked delays between them. Additionally, a change in the overall activation patterns can be seen. In general, all the plots show a smaller and steady slope when compared to the PS cases. The main reason is that the wavefront has to reach remote areas travelling only through the bulk myocardium.

The American Heart Association (AHA) 17 segment division was used to analyse the mean activation time on each LV region. Some of the information thus obtained is presented as bulls eye plots in Figure 4. Comparing the figures corresponding to the different geometries (Healthy, DCM, and HCM), it can be observed that the activation sequence of the segments of the LV lateral wall change their order of activation, which in physiological cases follow an apex to base pattern and now start from the LV lead position and spread towards base and apex. Moreover, comparing the cases with and without PS, a different behaviour is observed for the septal and for the lateral wall regions. The septal regions show shorter mean activation times with PS than without PS. On the other hand, the mean values for the lateral wall do not show noticeable changes. This leads to more synchronous activations in models with PS. It was further observed (not shown in the figures presented) that the mean activation times on the LV lateral wall are mainly dependent on the timing of the LV lead activation.

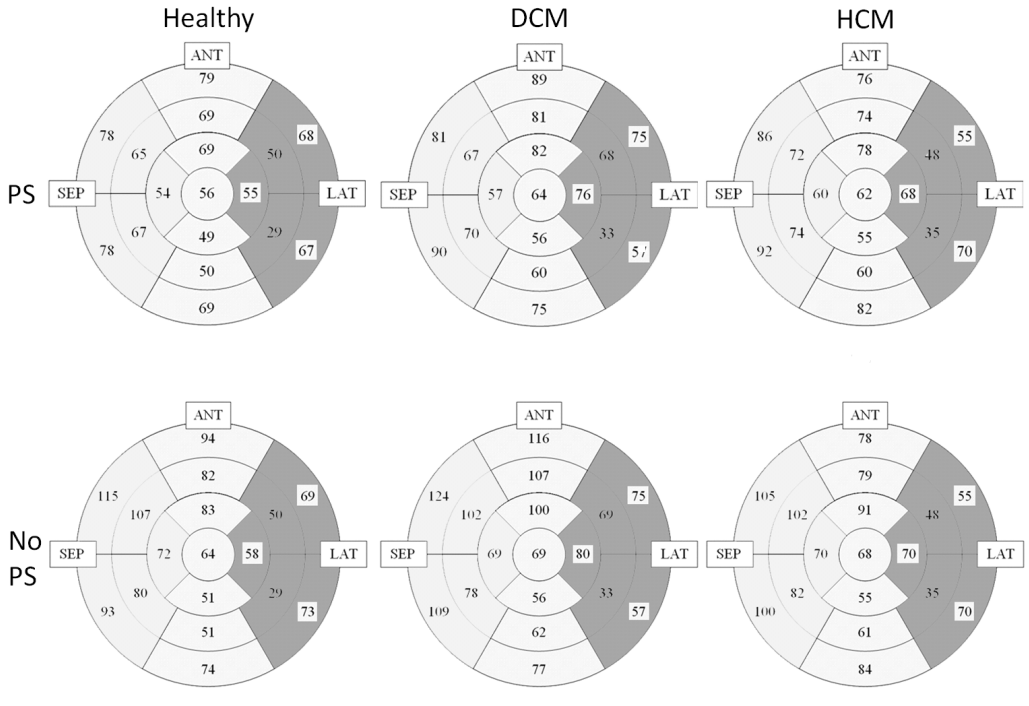

Fig. 4. Bulls eye plots of the 17 segments displaying the LV activation times for simultaneous pacing (VVD 0)

5 Conclusions

The importance of the PS in the electrical activation and its effect in CRT.

The analysis of the simulations performed on this study highlights the role of the PS and the specific cardiac geometry in the sequence of activation of the LV for different pacing strategies. The Purkinje system helps to minimize the intraventricular delay, so its appropriate activation synchronizes the septal and the LV lateral wall. Even though the importance of the PS in the electrical activation and its effect in CRT was shown, the PS model needs to be improved. The density of terminals in the system is probably low, leading to delays in the initial activation. A study to determine the accurate density of the PS is yet to be made.

The present study focused only on the electrical solution of the heart's activation, thus the mechanical feedback was neglected. Therefore, mechanical simulation should be included in the model in order to be able to refine the conclusions with regard to pacing therapies.

The influence of the geometry of the heart on the electrical activation pattern is highly relevant, as was pointed out. The wavefront generated from the LV lead, travelling from epicardium to endocardium, and the initiation of the PS retrograde conduction, are important variables on achieving an adequate pacing protocol. Structural changes that affect the LV size and thickness lead to a potential increase of intraventricular delays. Pacing on different geometries show variations in the activation sequences, specially on the LV lateral wall, in some cases differing significantly from the normal activation (apex to base).

Acknowledgments

This research has been partially funded by the Industrial and Technological Development Centre (CDTI) under the CENIT Programme (CDTEAM Project) and the European Community's Seventh Framework Programme (FP7/2007-2013) under grant agreement n. 224495 (euHeart project). Dr. R. Sebastian was funded by the Ministerio de Ciencia e Innovación (Juan de la Cierva program). Dr. B. Bijnens is an ICREA research professor at Universitat Pompeu Fabra. E. Vigmond and P.Boyle were funded by The Natural Sciences and Engineering Research Council of Canada. P. Boyle is supported by the Alberta Ingenuity Fund.

References

1. Henriquez, C., Papazoglou, A.: Using computer models to understand the roles of tissue structure and membrane dynamics in arrhythmogenesis. Proc. IEEE 84(3), 334–354 (1996)
2. Rodríguez, B., Li, L., Eason, J.C., Efimov, I.R., Trayanova, N.A.: Differences between left and right ventricular chamber geometry affect cardiac vulnerability to electric shocks. Circ. Res. 97(2), 168–175 (2005)

3. Durrer, D., van Dam, R.T., Freud, G.E., Janse, M.J., Meijler, F.L., Arzbaecher, R.C.: Total excitation of the isolated human heart. Circulation 41(6), 899–912 (1970)
4. Pollard, A.E., Burgess, M.J., Spitzer, K.W.: Computer simulations of three-dimensional propagation in ventricular myocardium, effects of intramural fiber rotation and inhomogeneous conductivity on epicardial activation. Circ. Res. 72(4), 744–756 (1993)
5. Weiss, D.L., Keller, D.U.J., Seemann, G., Dössel, O.: The influence of fibre orientation, extracted from different segments of the human left ventricle, on the activation and repolarization sequence: a simulation study. Europace 9 (suppl. 6), vi96–v104 (2007)
6. Sermesant, M., Delingette, H., Ayache, N.: An electromechanical model of the heart for image analysis and simulation. IEEE Trans. Med. Imaging 25(5), 612–625 (2006)
7. Reumann, M., Farina, D., Miri, R., Lurz, S., Osswald, B., Dössel, O.: Computer model for the optimization of av and vv delay in cardiac resynchronization therapy. Med. Biol. Eng. Comput. 45(9), 845–854 (2007)
8. Gassis, S., León, A.R.: Cardiac resynchronization therapy: strategies for device programming, troubleshooting and follow-up. J. Interv. Card. Electrophysiol. 13(3), 209–222 (2005)
9. Abraham, W.T.: Rationale and design of a randomized clinical trial to assess the safety and efficacy of cardiac resynchronization therapy in patients with advanced heart failure: the multicenter insync randomized clinical evaluation (miracle). J. Card. Fail 6(4), 369–380 (2000)
10. Chung, E.S., Leon, A.R., Tavazzi, L., Sun, J.P., Nihoyannopoulos, P., Merlino, J., Abraham, W.T., Ghio, S., Leclercq, C., Bax, J.J., Yu, C.M., Gorcsan, J., Sutton, M.S.J., Sutter, J.D., Murillo, J.: Results of the predictors of response to crt (prospect) trial. Circulation 117(20), 2608–2616 (2008)
11. Ordas, S., Oubel, E., Sebastian, R., Frangi, A.: Computational atlas of the heart. In: 15th International Symposium on Image and Signal Processing and Analysis. IEEE Computer Society, Los Alamitos (2007)
12. Camm, A.J., Lscher, T.F., Serruys, P. (eds.): The ESC Textbook of Cardiovascular Medicine. Wiley-Blackwell Publishing, Oxford (2006)
13. Sebastian, R., Ordas, S., Vigmond, E., Plank, G., Rodríguez, B., Frangi, A.: Assessing influence of conductivity in heart modelling with the aim of studying cardiovascular diseases. In: Proc. of SPIE Medical Imaging (2008)
14. Roberts, D.E., Scher, A.M.: Effect of tissue anisotropy on extracellular potential fields in canine myocardium in situ. Circ. Res. 50(3), 342–351 (1982)
15. Streeter, D.: Gross morphology and fibrous structure of the heart. In: Handbook of Physiology: The Cardiovascular System, vol. 1, pp. 61–112. Oxford University Press, Oxford (1979)
16. Plonsey, R.: Bioelectric sources arising in excitable fibers (alza lecture). Ann. Biomed. Eng. 16(6), 519–546 (1988)
17. Whiteley, J.P.: An efficient numerical technique for the solution of the monodomain and bidomain equations. IEEE Trans. Biomed. Eng. 53(11), 2139–2147 (2006)
18. Tusscher, K.H.W.J.T., Panfilov, A.V.: Cell model for efficient simulation of wave propagation in human ventricular tissue under normal and pathological conditions. Phys. Med. Biol. 51(23), 6141–6156 (2006)
19. DiFrancesco, D., Noble, D.: A model of cardiac electrical activity incorporating ionic pumps and concentration changes. Philos. Trans. R Soc. Lond. B Biol. Sci. 307(1133), 353–398 (1985)

20. Vigmond, E.J., Clements, C.: Construction of a computer model to investigate sawtooth effects in the purkinje system. IEEE Trans. Biomed. Eng. 54(3), 389–399 (2007)
21. Boyle, P., Deo, M., Vigmond, E.: Behaviour of the purkinje system during defibrillation-strength shocks. In: Proc. 29th Annual International Conference of the IEEE Engineering in Medicine and Biology Society EMBS 2007, pp. 419–422 (2007)
22. Vigmond, E.J., Hughes, M., Plank, G., Leon, L.J.: Computational tools for modeling electrical activity in cardiac tissue. J. Electrocardiol. 36(suppl.), 69–74 (2003)
23. Plank, G., Liebmann, M., dos Santos, R.W., Vigmond, E.J., Haase, G.: Algebraic multigrid preconditioner for the cardiac bidomain model. IEEE Trans. Biomed. Eng. 54(4), 585–596 (2007)

VI. Appendix II

Modeling the influence of the VV delay for CRT on the electrical activation patterns in absence of conduction through the AV node.

D A Romero, Rafael Sebastian, Gernot Plank, Edward J Vigmond and Alejandro F. Frangi.

in Proceedings of SPIE Medical Imaging. 2008, Vol. 6918, 69182G.

Modeling the influence of the VV delay for CRT on the electrical activation patterns in absence of conduction through the AV node

D A Romero*[a], Rafael Sebastián[a], Gernot Plank[b], Edward J Vigmond[c], Alejandro F. Frangi[a]
[a]Dep.Tecnologies de la Informació i les Comunicacions, Universitat Pompeu Fabra, Spain;
[b] Dep. of Biomedical Engineering, John Hopkins University, USA;
[c]Dep.of Electr. and Comput. Eng., University of Calgary, Canada;

ABSTRACT

From epidemiological studies, it has been shown that 0.2% of men and 0.1% of women suffer from a degree of atrioventricular (AV) block. In recent years, the palliative treatment for third degree AV block has included Cardiac Resynchronization Therapy (CRT). It was found that patients show more clinical improvement in the long term with CRT compared with single chamber devices. Still, an important group of patients does not improve their hemodynamic function as much as could be expected. A better understanding of the basis for optimizing the devices settings (among which the VV delay) will help to increase the number of responders. In this work, a finite element model of the left and right ventricles was generated using an atlas-based approach for their segmentation, which includes fiber orientation. The electrical activity was simulated with the electrophysiological solver CARP, using the Ten Tusscher *et al.* ionic model for the myocardium, and the DiFrancesco-Noble for Purkinje fibers. The model is representative of a patient without dilated or ischemic cardiomyopathy. The simulation results were analyzed for total activation times and latest activated regions at different VV delays and pre-activations (RV pre-activated, LV pre-activated). To optimize the solution, simulations are compared against the His-Purkinje network activation (normal physiological conduction), and interventricular septum activation (as collision point for the two wave fronts). The results were analyzed using Pearson's coefficient of correlation for point to point comparisons between simulation cases. The results of this study contribute to gain insight on the VV delay and how its adjustment might influence response to CRT and how it can be used to optimize the treatment.

Keywords: Heart Modeling, Therapy Planning, Cardiac Procedures, Cardiac Resynchronization Therapy, AV block.

1. INTRODUCTION

The VV delay is the time interval between the right (RV) and left ventricular (LV) stimulus set in biventricular pacemakers. Currently, its role in optimizing the outcome of patients with this therapy is subject of clinical studies. In this work, the population studied is narrowed to the pathological condition of no conduction through the atrioventricular (AV) node, as in the case in third degree (complete) AV block. It has been observed from an epidemiological study, that AV block affects 0.2% of men and 0.1% of women [1]. Nevertheless, a conduction block can also be induced by AV node ablation, as a palliative treatment for patients that combine chronic atrial fibrillation (AF) and heart failure (50% of patients in class IV of the NYHA (New York Heart Association) have AF) [2,3]. In these patients, the RV dual chamber pacemakers are currently being updated to CRT devices, since RV pacing can induce ventricular dyssynchrony in the long term [4,5]. Although Cardiac Resynchronization Therapy (CRT) positively effects the survival of these patients, some of them do not significantly improve their hemodynamic function [16]. Clinical trials to look for the best pacing setting for the VV delay have been performed, mostly using echocardiographic evaluation [6]. In recent years, methodologies based on intracardiac electrograms (IEGM) have emerged for delay assessment. It has been proposed that the optimal VV delay is achieved when the wave fronts from the RV and LV leads meet at the interventricular septum [7]. Another group states that the VV delay is optimized when the total activation time of the LV is minimized [8]. However, these techniques are not oriented to patients with an absence of conduction through the AV node.

*For further author information: (send correspondence to D.Romero)
daniel.romero@upf.edu; Telephone: +34 93 542 1451; Fax: +34 93 542 2517.

Medical Imaging 2008: Visualization, Image-guided Procedures, and Modeling, edited by
Michael I. Miga, Kevin Robert Cleary, Proc. of SPIE Vol. 6918, 69182G, (2008)
1605-7422/08/$18 · doi: 10.1117/12.770316

Using *in silico* experiments, we have simulated the performance of a CRT device in the setting of third degree AV block. This approach provides more electrical details on the activation patterns and was investigated at 2 different pre-activations with 3 delays for each, plus a simultaneous pacing and a physiological activation. The analysis was performed on the segmental activation, total activation time of the LV, the latest activated regions and the septal-lateral wall activation in absence of conduction through the AV node. Deeper knowledge on the activation patterns will contribute to refine the VV delay optimization methodologies and reducing the number of non-responders to the therapy.

A previous computational attempt has been made to optimize the VV delay during third degree AV block [17]. This group considers as their optimization criterion the highest resemblance between the isochrones of the resynchronized pathology and the isochrones of the physiological activation. In our work, we test a modified version of this criterion, comparing mean activation time of the regions in the 17 segments model [18], a graph that is more common in the clinical environment. The IEGM methods were also put to test. A patient's set of CT images was used to build the geometrical model. Patient specific models help personalize the treatment and improve the prediction of the hemodynamic outcome in a specific patient. The model accounts for anisotropic conduction and fiber orientation.

2. MATERIALS & METHODS

2.1. Model Construction

For our study, a 3D model of the heart was build which includes the LV and RV, and represents accurately the geometry of a patient. The particular geometry we adopted for the simulation study was segmented from a multi-detector computed tomography scan (MSCT) using an atlas-based approach [20]. The atlas of the heart, generated from 100 MSCT scans, including healthy and pathological patients, was able to adapt itself to our particular patient scan. As a result, a surface mesh of the patient, representing realistically its geometry was generated. Fig.1. shows the original CT images and the resulting 3D patient-specific surface mesh.

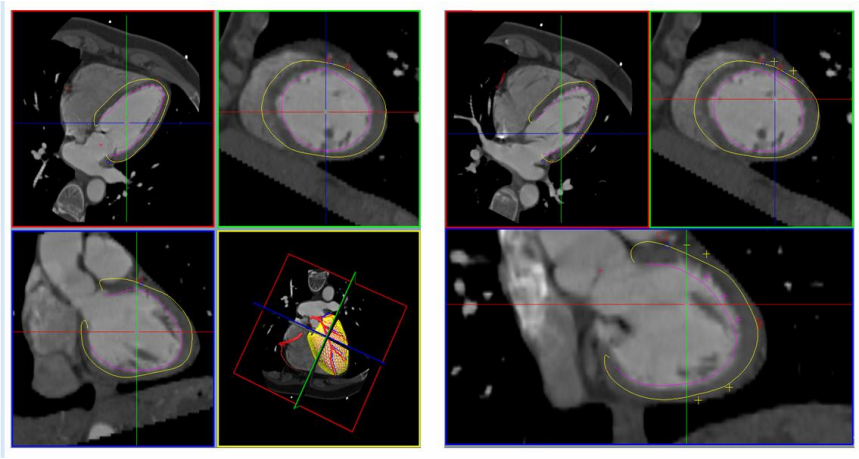

Fig.1. Ventricular segmentation by an atlas approach to the patient's geometry.

With the aim of carrying out patient-specific electrical simulations, we generated a volumetric finite element mesh (FEM) from the segmented heart geometry. The mesh was made up of tetrahedral elements and several restrictions were imposed to accomplish the size requirements needed for electrical simulation of heart tissue. In particular the maximum edge size of the elements was bounded to 500μm, which is in the order of the real elements we aim to model, and the edge-to-radius ratio limited to 1.2 to obtain regular shaped elements. With these constraints, the mesh had more than 14 million tetrahedral and 2.5 million nodes.

The model also included the myocardial fiber orientation and the His-Purkinje network, which are key structural elements to perform realistic electrical simulations. Fiber orientation was approximated by means of the Streeter's

conjecture [9], which has proven to be a good approximation [21]. The His-Purkinje network was manually delineated and included into the model following descriptions in the literature for normal hearts [19,24]. This network is a fast conduction system that plays a key role in the electrical activation of the heart in normal patients, and it is related to many important cardiac diseases such as left bundle branch block (LBBB).

2.2. Mathematical Modeling

The model is composed of two major components, a model for the ionic kinetics of the ventricular cells and a model of interconnection between cells. In this work, we make use of the Ten Tusscher model [14, 15] for the working myocardium, which represents a good balance between the level of electrophysiological detail and computational expense. It is mainly based on a quantitative description of ionic currents through the cell membrane from electrophysiological experiments and has been validated for human ventricular cells. The DiFrancesco-Noble model [13] was chosen for the cells of the Purkinje fibres.

The electrical propagation through cardiac tissue was simulated by means of the monodomain model. This model neglects the contribution of the extracellular domain, but in contrast, it reduces drastically the amount of time needed to perform a simulation. The parameter we used to model the passive tissue properties were assumed to be constant over time and space with C_m= 1μF/cm^2 and the set of longitudinal and transverse conductivities as reported by Roberts *et al.* [23].

2.3. Simulations design

A simulation study was designed with the aim of testing several settings of the CRT devices commonly used in clinical practice for patients showing AV block. Our model is representative of a patient without ischemic or dilated cardiomyopathy. This is assured by normal physiological geometries for the left and right ventricle as well as the conductivity of the myocardium being within normal values. Both conductivity and geometry are kept constant for all the simulations. The initiation of the heart depolarization is triggered by means of an intracellular sock that represented the effect of leads used for CRT. The electrode positions are fixed for all the simulations at the RV endo-apex and LV epi-lateral wall. The electrode size corresponds to the number of nodes being stimulated within a volume of 1.5x1.5x1.5mm^3 for each electrode, intensity (0,002μA/cm^3, transmembrane current), and time step of the stimulus (2ms).

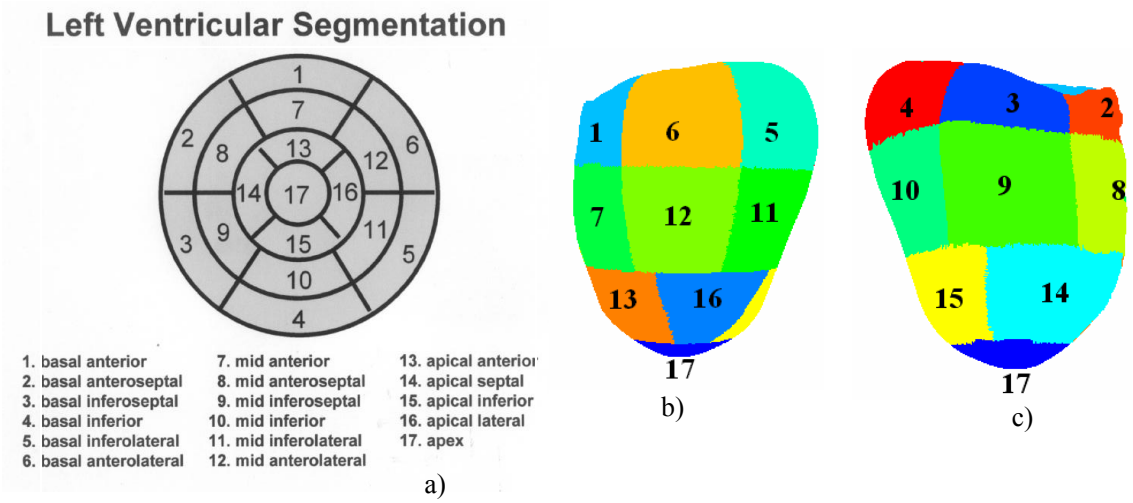

Fig.2. a) The AHA 17 segment model for myocardial segmentation. Figure modified from [18]. b) and c) are the antero-lateral and postero-septal views respectively of the 17 segment model in 3D left ventricle.

Two simulations were performed as baseline for comparison: physiological activation through the His-Purkinje network, and simultaneous pacing (VV delay = 0). For VV delays different from zero there will be two categories: RV pre-activated and LV pre-activated. The VV delays were set for 10, 20 and 30ms. Notations used in this paper to indicate the

simulations are the pre-activated ventricle followed by the delay for the other ventricle activation. For example, LV10 means LV pre-activation with a VV delay of 10ms. In the case of simultaneous pacing, the LV0RV notation is used.

The IEGM criterions for reducing total activation time and septum activation [7,8] were tested while searching for the optimum delay from resynchronization cases. To facilitate the interpretation of the results, the LV ventricle volumetric mesh was divided into 17 segments according to the AHA standardized myocardial segmentation and nomenclature (see Fig.2. (b) and (c)).

3. RESULTS

A total of eight patient specific simulations were run. From the visual inspection of the isochrones, it was clear that the criterion of wavefronts was never achieved, for the chosen delays. Fig.3 shows the isochrone maps of the late activation time (LAT), which is the time measurement of the local activation referenced to time zero. Each color in the maps represents a 10ms interval, time zero beginning at the first paced stimuli. For simultaneous pacing (Fig.3. (c) and (d)), the collision site occurred at the apical lateral segment (segment 16) and slightly anterior (segment 13), while for RV pre-activated cases, it moved laterally and correspondingly septal for LV pre-activations. See Fig.3.

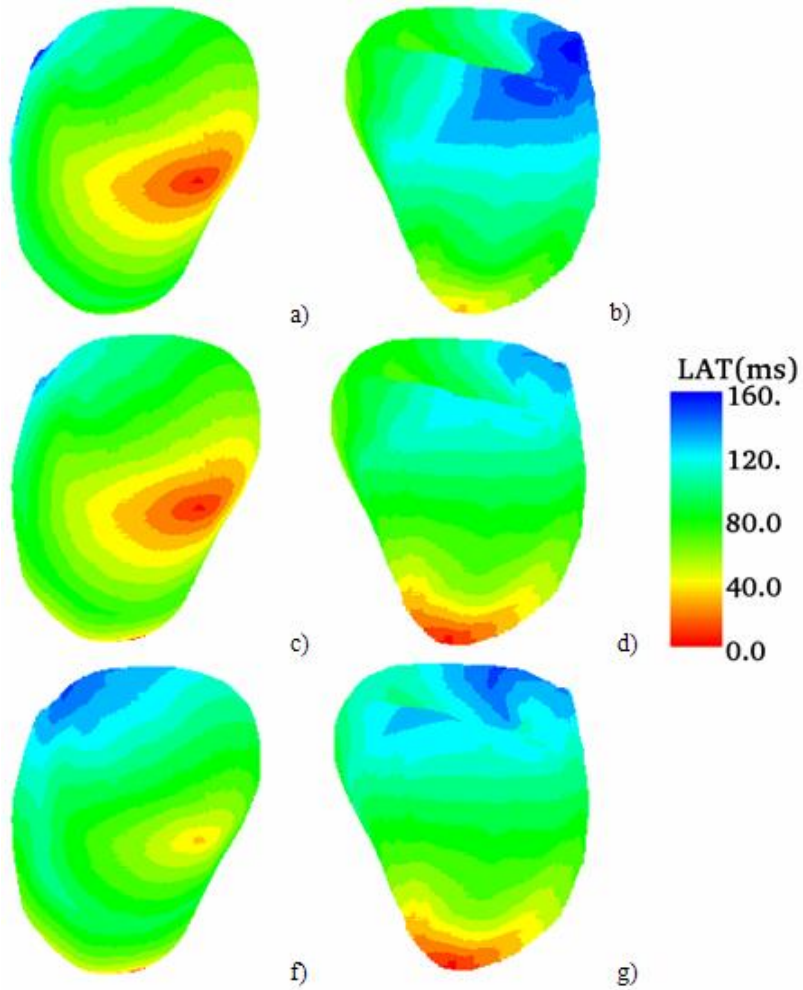

Fig.3. Isochrone maps. a) and b) LV30. c) and d) LV0RV. f) and g) RV30. a), c) and f) projections were taken from an anterior-lateral view. b), d) and g) projections were taken from a septal view.

The total activation times (TAT) showed high values and a relatively low variability. This is explained by a lack of retrograde conduction in Purkinje fibers, which was not accomplished in our simulations. The best resynchronization was set for the simultaneous pacing (see Table 1.). For the Purkinje network activation a TAT of 92ms is nearly above physiological values.

In clinical practice, a well-established criterion for defining delays involves the use of echocardiography to obtain the most simultaneous activation (contraction) of the lateral wall and the septum [6]. We employed this technique for analyzing the activation of the ventricles throughout the simulations. The segments used to define lateral wall were segments 11, 12 and 16 as for septal segments 8, 9 and 14.

Table 1. Total Activation Times (ms)

Purkinje	LV30	LV20	LV10	LV0RV	RV10	RV20	RV30
92	156	152	143	135	138	142	147

As a method for quantifying the variance in septal-lateral activation, we used the activated nodes relative cumulative frequency. This measurement is an indication of how quickly a wall activate. It refers to the number of nodes that have activated before a certain moment in time. Two advantages of this technique are its independence from the number of nodes (since it is normalized), and its space distribution.

The two curves obtained were compared using Pearson's correlation coefficient (ρ). The high similarity between the curves was a factor that raised the coefficients strongly. For this reason, a more appropriated method is quantifying the area between the curves.

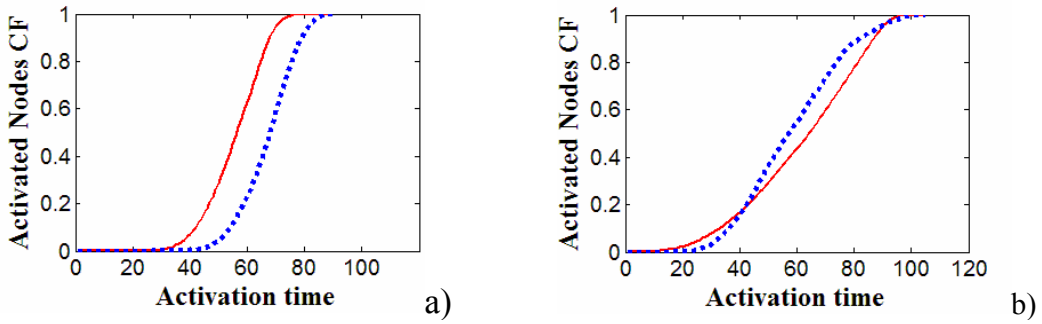

Fig.4. Activated Nodes Cumulative Frequency (CF). a) Purkinje network activation. b) RV20. The red continuous line presents the septal activation, and the blue dashed line is the lateral's wall activation.

Correlation coefficients and area measurements are shown in Table 2. The best correlation coefficient was obtained at RV30. Still, the area analysis shows the higher septal-lateral activation similarity at RV20. Taking into the account the inconvenience of the correlation stated before, the optimum solution is RV20 (Fig.4. (b)).

The septal-lateral activation difference in the Purkinje case (Fig.4. (a)) corresponds to earlier septal activation, caused by the firsts LV breakthroughs being near the anterior paraseptal, mid septum and posterior paraseptal within the first 5ms after the first endocardial activation, as reported by Durrer *et al*.[19]. Nonetheless, a fine tuning of the conductivities in the model should allow us to decrease the actual activation difference in the Purkinje simulation.

The 17 segment analysis for all resynchronizations with LV pre-activation showed that the basal anteroseptal and basal anterior segments (segments 1 and 2) were the latest activated regions. In RV pre-activation, the latest segment was basal anterior. The segments defined by us as the septal wall (8, 9 and 14) kept a 10ms delay between their activation, subject to their respective delay (see Fig.5.). This confirms the RV apex stimulus as the only source for septal activation, and is reaffirmed by the fact that in RV pre-activated cases the mean activation time of these segments remains constant. The same occurred for the lateral wall (segments 11, 12 and 16), which activation only originated from the LV electrode. See Fig.6.

Table 2. Septal-Lateral Activation Analysis

	Purkinje	LV30	LV20	LV10	LV0RV	RV10	RV20	RV30
ρ (Septal vs. Lateral)	0,933	0,688	0,763	0,838	0,905	0,958	0,990	0,994
Area (Septal vs. Lateral)	11,518	52,195	42,597	32,766	22,923	13,134	**3,421**	6,226
RMSE (Purkinje)	-	38,060	34,797	31,634	***28,853***	29,373	30,719	32,705
RMSE (Optimum)	-	20,377	16,120	12,908	12,205	5,978	-	5,764

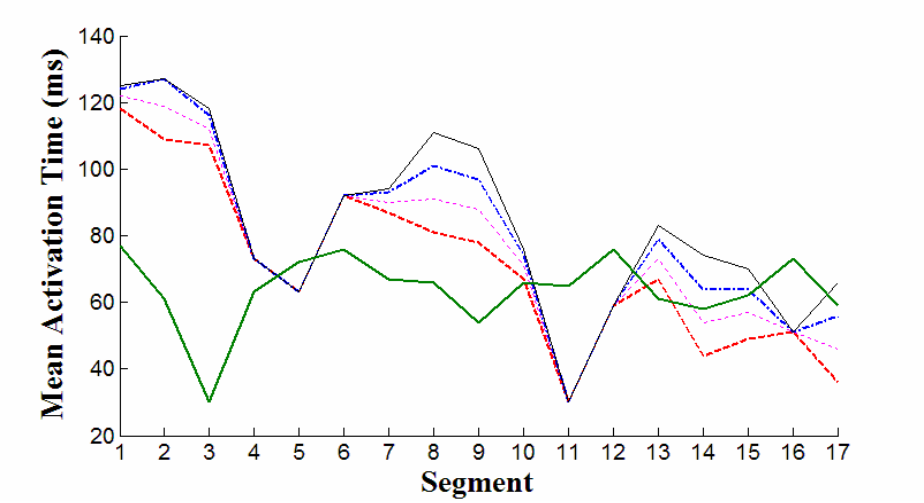

Fig.5. Segmental activation of the LV pre-activated cases. LV10 magenta dotted line. LV20 blue dot-dash line. LV30 black continuous line. LV0RV (red dash-dot line) and Purkinje activation (green continuous line) were also plotted for comparison and a visual referent.

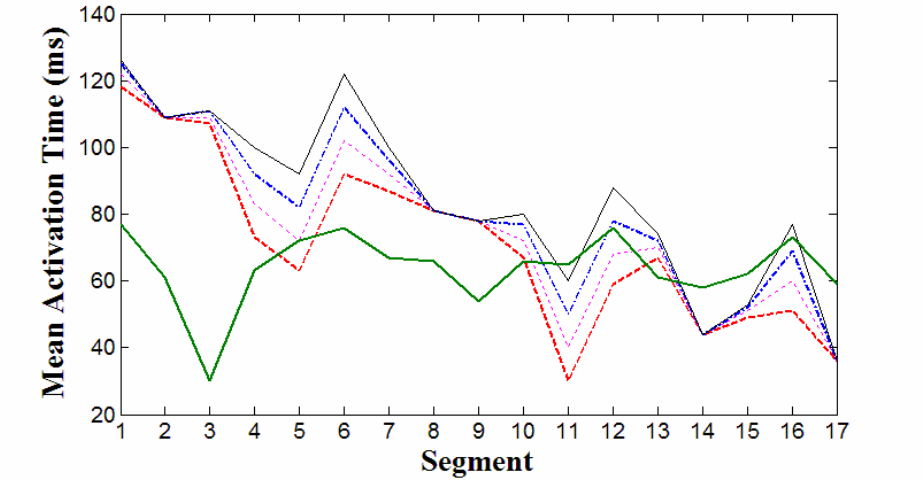

Fig.6. Segmental activation of the RV pre-activated cases. RV10 magenta dotted line. RV20 blue dot-dash line. RV30 black continuous line. LV0RV (red dash-dot line) and Purkinje activation (green continuous line) were also plotted for comparison and a visual referent.

Using RV20 as the best solution for the therapy, we compared the activation pattern by calculating the root mean square error (RMSE) between the mean activation time per segment from the rest of the cases and this solution. The RMSE has been previously used as an optimization method in similar work by other groups [17,22]. The same was applied using the Purkinje network activation as the optimum solution. Results are presented in Table 2. As expected, the lowest error is

obtained near RV20, while the RV20 activation pattern still holds more similarity to RV30 than RV10. Using the Purkinje network, the lowest error was obtained at simultaneous pacing.

4. CONCLUSIONS

Current criteria for CRT optimization based on IEGMs were tested in our simulations for the case of absence of conduction through the AV node, for which the criteria have not yet been established. Both the total activation time criterion and the lowest RMSE, when compared to the Purkinje network activation, showed simultaneous pacing as the optimal solution. While others recommended the collision of the activation wavefronts, coming from each electrode, at the septum as the optimal solution, in our simulations (of a resynchronized AV block), this was never observed.

A third criterion, widely used in clinical practice, suggesting the most simultaneous contraction of the septal and lateral walls as optimal, was extrapolated to its electrical nature. Using this criterion, the best solution was found to be at the RV pre-activated with a 20ms delay. This simulation presents the second furthest collision site from the septum and ranks as the third option by its total activation time after the simultaneous pacing.

The activated nodes relative cumulative frequency proves to be a promising tool aiding the optimization of the Cardiac Resynchronization Therapy. Future work will test this approach on endocardial surface maps, which are the available data in clinical practice. Future simulations will also test the influence of different LV lead positions on the optimal solution.

Achieving retrograde conduction through the Purkinje fibers will reduce the total activation time of the LV, producing a more accurate solution for the resynchronization. The current model also enables us to include ischemic regions in the myocardium and we intend to work on this to assess the treatment of heart failure patients with underlying coronary artery disease.

As computer modeling of the heart activity evolves into a more refined and robust technique, the possibilities and reliance on *in silico* trails will help to optimize clinical trials. Simulation studies on the VV delay, and how to optimize it in a clinical setting are likely to increase our understanding of the therapy and will contribute to increasing the number of responders to CRT.

5. ACKNOWLEDGEMENTS

D. Romero, R. Sebastian and A. Frangi have been partially funded by the Industrial and Technological Development Centre (CDTI) under the CENIT Programme (CDTEAM Project) and the Networking Research Center on Bioengineering, Biomaterials and Nanomedicine (CIBER-BBN). G. Plank was supported by a Marie Curie Fellowship MC-OIF 040190 from the European Commission and the SFB grant F3210-N18 from the Austrian Science Fund FWF. E. Vigmond was funded by The Natural Sciences and Engineering Research Council of Canada.

6. REFERENCES

1. De Bacquer D, De Backer G, Kornitzer M. Prevalences of ECG findings in large population based samples of men and women. *Heart* 2000;84:625–633.

2. Kiès P, Leclercq C, Bleeker G B, *et al*. Cardiac resynchronisation therapy in chronic atrial fibrillation: impact on left atrial size and reversal to sinus rhythm. *Heart* 2006;92:490-494.

3. Hoppe Uta C, Casares Jaime M,Eiskjær Hans, *et al.* Effect of Cardiac Resynchronization on the Incidence of Atrial Fibrillation in Patients With Severe Heart Failure. *Circulation* 2006;114:18-25.

4. Gregoratos G, Abrams J, Epstein AE, Freedman RA, *et al*. ACC/AHA/NASPE 2002 guideline update for implantation of cardiac pacemakers and antiarrhythmia devices: a report of the American College of

Cardiology/American Heart Association Task Force on Practice Guidelines (ACC/AHA/NASPE Committee on Pacemaker Implantation). *J Am Coll Cardiol* 2002.

5. Thambo JB, Bordachar P, Garrigue S, Lafitte S, *et al.* Detrimental Ventricular Remodeling in Patients With Congenital Complete Heart Block and Chronic Right Ventricular Apical Pacing. *Circulation* 2004;110:3766-3772;

6. Sogaard Peter, Egeblad Henrik, Pedersen A K., *et al.* Sequential Versus Simultaneous Biventricular Resynchronization for Severe Heart Failure: Evaluation by Tissue Doppler Imaging. *Circulation* 2002;106:2078-2084.

7. Goscinska-Bis K, Grzegorzewski B, Migschitz Mario, *et al.* Intracardiac electrogram method of VV-delay optimization in biventricular pacemakers. *Cardiol J* 2007; 14: 305.310

8. Min Xiaoyi, Meine Mathias, Baker James H, *et al.* Estimation of the Optimal VV Delay by an IEGM-Based Method in Cardiac Resynchronization Therapy. *PACE 2007; 30:S19–S22*

9. Streeter D D. Gross morphology and fibre geometry of the heart. In: Berne RM, Sperelakis N, Geiger SR eds) *Handbook of Physiology*. *The cardiovascular system*. Williams & Wilkins, Baltimore, 1979; pp 61–112.

10. Vigmond E J, Hughes M, Plank G, Leon L J. Computational tools for modeling electrical activity in cardiac tissue. *Journal of Electrocardiology* 2003;36:69–74.

11. Noble D and Rudy Y. Models of cardiac ventricular action potentials: iterative interaction between experiment and simulation. *Phil. Trans* 2001;359:1127–1142.

12. Henriquez C S and Papazoglou A A. Using computer models to understand the roles of tissue structure and membrane dynamics in arrythmogenesis. *Proceedings of IEEE* 1996;84:334–354.

13. DiFrancesco D and Noble D. A model of cardiac electrical activity incorporating ion pumps and concentration changes. *Phil. Trans. Roy. Soc.* 1985;307:353–398.

14. Ten Tusscher K H W J, Noble D, Noble P J. Panfilov. A V. A model for human ventricular tissue. *Am J Physiol Heart Circ Physiol*, 2004;286:1573–1589.

15. Ten Tusscher K H W J and Panfilov. A V. Cell model for efficient simulation of wave propagation in human ventricular tissue under normal and pathological conditions. *Physics in Medicine and Biology* 2006;51:6141–6156.

16. Abraham William T and Yancy Clyde W Jr. Cardiac Resynchronization Therapy: A Practical Guide for Device Optimization, Part I. *CHF* 2006;12:169–173.

17. Reumann M, Farina D, Miri R, Lurz S, Osswald B, Dössel O. Computer model for the optimization of AV and VV delay in cardiac resynchronization therapy. *Med Bio Eng Comput* 2007; 45:845–854.

18. American Heart Association, American College of Cardiology, and Society of Nuclear Medicine. Imaging guidelines for nuclear cardiology procedures, Part 2. *J Nucl Cardiol* 1999;6:G47-G84.

19. Durrer D, Van Dam R Th, Freud G E, Janse M J, Meijler F L, Arzbaecher R C. Total Excitation of the Isolated Human Heart. *Circulation* 1970;41:899-912.

20. Ordás S, Oubel E, Sebastián R, Frangi A.F. Computational atlas of the Heart. *15th International Symposium on Image and Signal Processing and Analysis*. IEEE Computer Society, 2007.

21. Jouk P S, Mourad A, Milisic V, Michalowicz G, Raoult A, Caillerie D, Usson Y. Analysis of the fiber architecture of the heart by quantitative polarized light microscopy. Accuracy, limitations and contribution to the study of the fiber architecture of the ventricles during fetal and neonatal life. *Eur J Cardiothorac Surg* 2007;31:915-921

22. Muzicant, A.L., Henriquez, C.S. Validation of three-dimensional conduction models using experimental mapping: are we getting closer?, *Progress in Biophysics and Molecular Biology*1998;69:205–223,.

23. D. Roberts and A.M. Scher, Effect of tissue anisotropy on extracellular potential fields in canine myocardium in situ, *Circ. Res*1982: 50;342–351.

24. Pollard A E, Barr C. The construction of an anatomically based model of the human ventricular conduction system. *Biomed. Eng IEEE Trans* 1990;37: 1173–1185.